Materials & Design 234 (2023) 112329

Contents lists available at ScienceDirect

Materials & Design

journal homepage: www.elsevier.com/locate/matdes

Nanoscale printed tunable specimen geometry enables high-throughput miniaturized fracture testing

Alexander Jelinek [a,*], Stanislav Zak [b], Megan J. Cordill [b], Daniel Kiener [a], Markus Alfreider [a]

[a] Department of Materials Science, Montanuniversität Leoben, Franz-Josef-Straße 18, 8700 Leoben, Austria
[b] Erich Schmid Institute for Materials Science, Austrian Academy of Sciences, Jahnstraße 12, 8700 Leoben, Austria

ARTICLE INFO

Keywords:
Two-photon lithography
Push-to-pull devices
Micromechanics
Essential work of fracture
High-throughput testing
Double edge notched tension

ABSTRACT

Two-photon lithography (TPL) enables the design of novel micromechanical specimens, down to sub-micron resolution, thus extending the possibilities for device and material characterisation and pushing the boundaries of a broad range of miniaturized technologies such as optics, analytics, and medicine. Employing a push-to-pull geometry, incorporating double edge notched tension specimens loaded in mode I, the specimen manufacturing and testing can be automated to a large extent. This allows for the use of large parameter space characterisation methods as the essential work of fracture, with an experimentally simpler to realize compression testing setup. Within this work, a methodology is outlined for automated specimen direct laser writing with a TPL-device and subsequent testing via a nanoindenter. In total, 2100 specimens were manufactured, of which 1997 could be used for evaluation. Estimations for the essential work of fracture of the used photoresist is presented, with regards to influencing parameters such as testing displacement rate and laser writing power. A discussion of its statistical robustness and validity considerations is included. This will act as a basis framework for further statistical fracture evaluation schemes for other resin materials, as well as for probing thin film systems.

1. Introduction

Direct laser writing via two-photon lithography (TPL) is a promising key technology for manufacturing of small-scale devices in various applications. Due to the utilization of established photo resin formulations, a broad range of printable polymers is already available, not limited to common photoresists. Polymers with tuned optical properties enable the direct writing of optical wave guides [1–5] or the coupling of optical fibres [6–9] to photonic circuits made from semiconductors [10–14], including common 2D lithographic technology and breaching the gap towards integrated photonic circuits [15]. Furthermore, diffractive and refractive optical parts [16–19] can be directly printed on top of optical fibres, opening new possibilities for small-scale analytical [20–24] and minimally invasive medical devices [25]. Additionally, the nontoxic or even biocompatible character of photopolymers comes into consideration, since it allows the direct contact of printed parts with body tissue [26–28] or cells [29–31]. These combined properties are vital for lab-on-a-chip applications, [32,33] for example where very small liquid flows are pumped through micro fluidic channels [34–36] and operative devices [37] for analysis and *in vivo* studies. Recently, even more advanced testing devices for heart tissue [38,39] were developed, where besides the biochemical environment even the mechanical stimulus could be applied to living and growing cells.

However, many applications deal with a mechanical load to a certain extent due to thermal mismatches between adjacent materials, pressure gradients, direct straining, or shrinkage by ageing, to name a few. The resulting stress will induce deformation due to comparably low Young's modulus or might lead to a failure if yielding or fracture takes place within critical parts manufactured by direct laser writing. As a countermeasure, the design could be optimized to avoid stress concentrations. Finite element (FE) analysis might also be helpful in special cases, as common in larger scale manufacturing, since the digital model is already available from the print job. In any case, knowledge of the basic mechanical properties such as Young's modulus and yield strength is vital. As these values are strongly dependent on the processing parameters [40], it is necessary to probe them in the motive processing conditions. For more advanced considerations also fracture related properties are of interest, especially if material failure should be prevented and reliability is of importance. Notably, the testing procedure might be more demanding. The relation of basic mechanical properties to the environmental history - meaning UV-radiation [41], humidity,

* Corresponding author.
E-mail address: alexander.jelinek@unileoben.ac.at (A. Jelinek).

https://doi.org/10.1016/j.matdes.2023.112329
Received 1 May 2023; Received in revised form 14 September 2023; Accepted 15 September 2023
Available online 16 September 2023

Nomenclature

TPL	Two-photon lithography
FE	Finite element
PTP	Push-to-pull
DENT I	Double edge notched tension specimen in mode I
EWF	Essential work of fracture (method)
DC	Degree of conversions
SEM	Scanning electron microscope
FIB	Focused ion beam
CAD	Computer aided design
W_f	Total work of fracture
W_e	Essential work of fracture
W_p	Non-essential work of fracture
l	Ligament length
t	Ligament thickness
β	Fracture geometry parameter
w_f	Specific work of fracture
w_e	Specific essential work of fracture
w_p	Specific non-essential work of fracture
S_{EI}	Standard error of the y-intercept
S_{ES}	Standard error of the slope
t_α	Student's factor
n	Statistical sample size
α	Probability level (here $\alpha = 5\%$)
E	Young's modulus
σ_y	Yield strength
r_p	Plastic zone radius
J_i	J-integral at critical crack initiation
K_{FE}	Stress intensity factor for mode I fracture (by FE simulation)
K_{we}	Stress intensity factor translation of w_e values
$K_{Q,FE}$,	Conditional fracture toughness (mean value of multiple K_{FE})
w_i	Elastic strain energy density
ε	Strain
W_i	Initially present strain energy
L	Length of the specimen
W	Width of the unnotched specimen
σ_N	Cross-sectional net stress at maximum force
F_{max}	Maximum force

and most prominently elevated temperature, adds additional challenges for comprehensive material characterisation.

With small-scale material testing techniques [42], fundamental mechanical properties [43] can be accessed and the quantitative determination of post-curing, aging, and degradation effects [44] is enabled, directly on material samples produced by TPL [45], therefore avoiding correlative estimations based on e.g. polymer chemistry and cross-linking density. With miniaturized standard bending [46], tension [47,48] or compression [49–53] tests, Young's modulus and yield strength are obtained, whereas the determination of Poisson's ratio [46] and fracture properties [54–57] require dedicated geometries. In the case of fracture mechanical specimen, there are many methods available, reaching from basic notched tension specimens to cantilever bending or pillar splitting. Since direct laser writing enables the manufacture of relatively complex shapes, testing geometries are not limited to the cuboidal or cylindrical shapes commonly obtained by small-scale milling processes. Thus, the geometry can be designed directly for the specific needs of testing, in contrast to the usual approaches. In fact, a specific push-to-pull (PTP) specimen geometry based on classical theta specimen was developed [58,59], enabling to perform mechanistically preferred tension experiments with an experimentally less demanding compression loading setup. In principle, a kinematic relation is utilized, where the compression force (and displacement) on top is translated to symmetrical outside bending of struts, thereby tensioning the actual specimen geometry in between. Other authors already used original theta geometries on a small-scale for films deposited on silicon [60] or differently adapted PTP geometries for testing coated specimens [61], as even thin coatings with stiff materials considerably improve the stability of the structures [62,63].

The aim of this work is to establish an equally simple, but slightly tuned version incorporating a double edge notched tension specimen in mode I (DENT I) for compression loading. The DENT I geometry is a well-documented specimen shape with all relevant fracture mechanical formulation developed [64]. A key advantage of the DENT I specimen geometry is its symmetry, which leads to confinement of the plastic zone and all potentially crack associated zones between the two notches. Furthermore, due to the pure tension loading, criticality within the ligament region can be maintained during formation of a crack or plastic zone. For the presented specimen geometry such a DENT I shape is positioned inside a PTP frame in a way to perform high fidelity *in situ* experiments within a scanning electron microscope (SEM) as well as for high throughput *ex situ* testing via a nanoindenter devices, as depicted in Fig. 1**(a)**. A preliminary design and successful initial testing were already presented in a previous publication [65]. Otherwise, a reduction scheme, as sketched in Fig. 1**(b),** must be applied for subtracting the PTP frame contribution (in terms of force) to the initial force vs. displacement data (described in detail later). With this information, an elastic–plastic fracture-energy-based J-integral evaluation can be performed already.

Through this work, the possibility of specimen production by direct laser writing is extended to perform a comprehensive material characterization in terms of the essential work of fracture (EWF) approach [66–68]. The EWF evaluation, originally developed for thin sheets of steel [69], gained much attention for testing of thin polymer sheets [70]. It is an energy-based multi-specimen approach and requires specimens with different initial ligament sizes, exhibiting plane stress dominated crack growth. In principle, the fracture zone is divided into two parts as depicted in Fig. 1**(c)** the inner fracture process zone, where the energy for driving crack growth and creation of new surface is consumed, and the outer fracture process zone, where the non-essential work of fracture is dissipated. For ductile metals, the non-essential work is mainly consumed by plastic deformation, whereas for polymeric materials, different mechanisms such as disentanglement of the polymer network, crazing, and/or chain-bridging, can operate depending on the microstructure [71]. Starting from the total work of fracture, W_f, obtained by integration of the force vs. displacement graph as sketched in Fig. 1**(d)**, of specimens with various ligament lengths l, the fracture area specific work of fracture w_f is derived. If w_f is plotted against l as in Fig. 1**(e)**, the essential and non-essential work of fracture, w_e and βw_p, is obtained by linear regression in a final step.

In order to apply the EWF approach, specimen variations with different ligament sizes were constructed and automatically manufactured by a TPL-printer via a writing script, which enabled to back the results by a statistically relevant number of specimens. To the best knowledge of the authors, new aspects of this small-scale high-throughput testing scheme presented to the scientific community for the first time. A large amount of complex shaped specimen is utilized, which would not be possible to manufacture without TPL in a reasonable way. Furthermore, a general evaluation framework for such PTP specimens is derived. The testing was performed in an automated manner with the use of nanoindentation over a specified grid. In the future the methodology can be conveniently extended to further resists, specifically aged

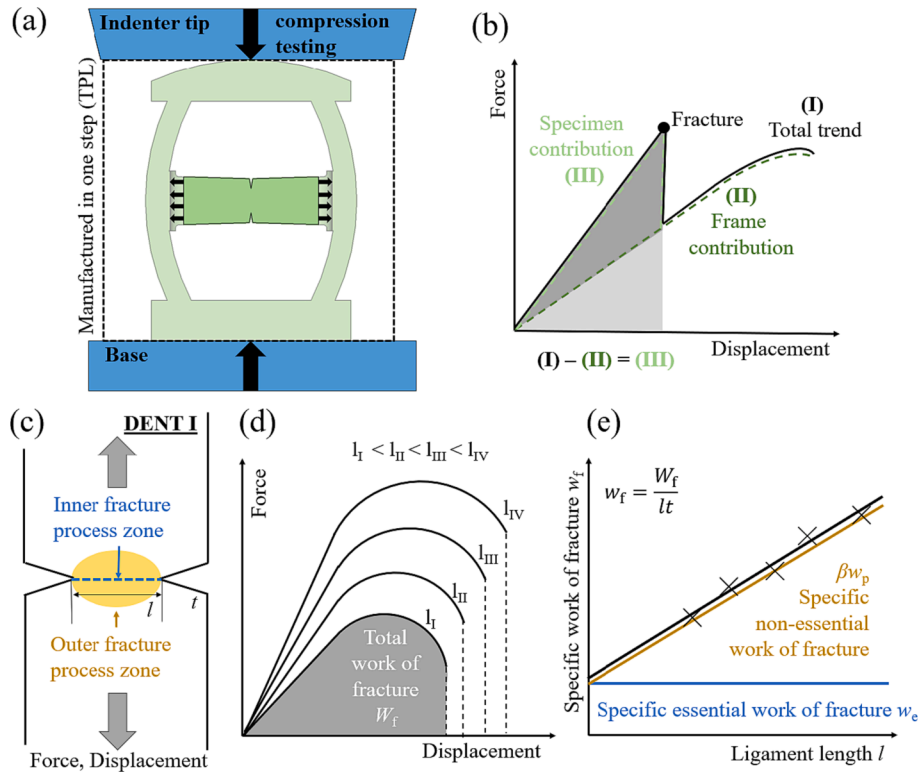

Fig. 1. Schematic sketch of (a) compression testing a PTP frame (lighter green) incorporating a DENT I specimen geometry (obtained by TPL, darker green) via a flat-punch indenter tip. With (b) idealized force vs. displacement graph consisting of specimen and frame contribution, including the fracture event. Via force correction for the frame contribution, the pure specimens signal is obtained. For evaluation an EWF approach is utilized, (c) discriminating between inner and outer fracture process zone. (d) The force vs. displacement graph of specimens with increasing ligament sizes shows an increasing total work of fracture, which is (e) plotted normalized via the geometry over the ligament length to finally obtain the essential and non-essential work of fracture by linear regression. (For interpretation of the references to colour in this figure legend, the reader is referred to the web version of this article.)

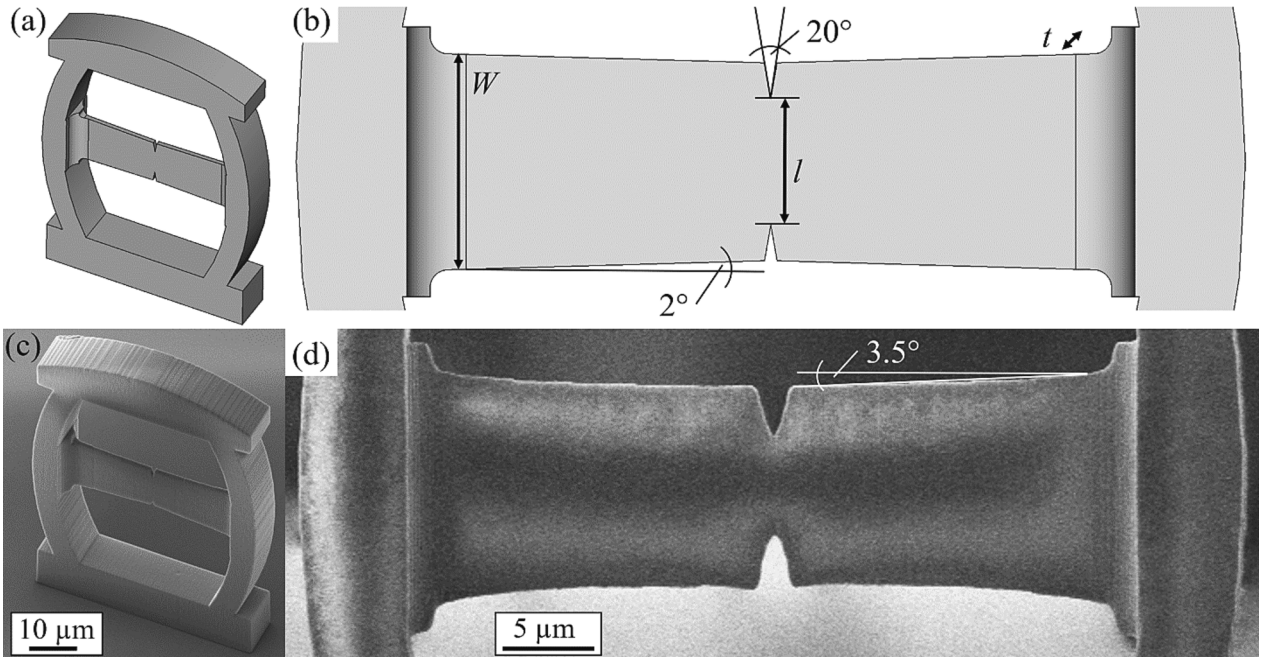

Fig. 2. Digital model (a, b) and print (c, d) of a push-to-pull device incorporating a double edge notched tension specimen. (a) Overview with rounded top face, where the force is applied, (b) DENT I fracture specimen with corresponding dimensions. The values depend on writing parameters and ligament type (see supplementary Table T1). (c) and (d) SEM images under corresponding viewing angles. Specimen imperfections are visible in (d), especially near the notch regions, as small steps or rounded edges due to the laser writing process.

specimens or to other similarly processed materials. Also, variation of environmental conditions in terms of humidity or temperature presents a rather straight forward future task.

2. Experimental methodology

2.1. Specimen design

The specimen design was inspired by previous realisations of push-to-pull concepts on silicon [60], but slightly adapted for direct view on the incorporating testing geometry. The present design, shown in Fig. 2**(a)** as a 3D model and **(c)** as a real print, consists of a base and a rounded top-block, connected by struts. These bend out during compression loading from the top and translates the force to tension inside the specimen geometry through a kinematic relation. Here, a common DENT I shape was used (see Fig. 2**(b)**) to promote symmetric failure in the very centre of the whole device. In a previous work [65], a linear elastic FE analysis revealed a slightly higher stress intensity on the upper notch. However, the minor deviation is negligible with respect to the overall fracture parameter evaluation as shown herein.

A slight inclination of 2° on faces facing downwards was found to eliminate printing artefacts originating from large overhanging layers. This taper is introduced on all horizontally depicted faces (see Fig. 2**(b)**) to preserve specimen symmetry. Slight printing deviation led to a taper of 3.5° as shown in Fig. 2**(d)**. Further details on the designing approach, as well as an estimation of geometry factors for a basic linear elastic fracture evaluation can be found in a previous publication [65]. As the EWF approach requires different ligament sizes, five versions of the specimen geometry were designed (l = 3, 4, 5, 6, 7 μm), with symmetrically decreasing notch depths. For the digital construction, the CAD software FreeCAD (version: 0.18, Debian GNU/Linux) was used.

2.2. Specimen writing via two-photon-lithography

For specimen fabrication, the TPL system PPGT 2 (Photonic Professional GT2, NanoScribe GmbH & Co. KG, Eggstein, Leopoldshafen, Germany) with the associated small features solution set was used, consisting of a 63x Objective (Plan-Apochromat 63x N.A. 1.4 Oil DIC, Carl Zeiss AG, Oberkochen, Germany), the negative-tone photoresist IP-DIP (Nanoscribe GmbH & Co. KG, Eggstein-Leopoldshafen, Germany) and 1'' x 1'' fused-silica substrates.

For the special case of SEM *in situ* experiments, the substrates were prepared to allow for perpendicular imaging as follows. Pre-cuts with a diamond wire saw (type: 6234, well Diamantdrahtsägen GmbH, Mannheim, Germany), were applied to a depth of about 300 μm, to which edges of the specimen were later printed. After the printing procedure (described in more detail below), a hard metal scribing tool was used to make scratches within the sawing grooves, which act as pre-cracks for manual splitting of the substrate into 5 × 5 mm^2 plates.

A silanization procedure was applied to enhance the adhesion of the printed polymer to the substrate surface [72]. Therefore, the substrates were subjected to corona-plasma activation (custom built, Ahlbrandt System GmbH, Lauterbach, Germany), directly followed by submersion in a silane solution (27 ml ethanol (100%), 3 ml distilled water, 5 drops of glacial acetic acid and 300 μl 3-(Trimethoxysilyl)propyl acrylate (CAS:4369–14-6)) in a tape-sealed glass Petri dish for 24 h at 70 °C. Subsequently, the already hydrophobic plates were rinsed with ethanol, dried, and baked at 180 °C for another 8 h. The substrates were drily stored at room temperature within a desiccator until usage.

For the preparation of the print files via the printer's associated software, a slicing distance of 100 nm was used with hatching of 200 nm and with a shifted scanning direction of 90° between each printed layer. For the scanning speed the standard of 10 mm/s was kept, but the writing laser power parameter was adjusted to 50, 55 and 60 for specific specimen sub-sets, corresponding to 25, 27.5 and 30 mW, respectively. After writing, the standard development procedure with submersion in propylene-glycol-methyl-ether-acetate for 20 min and isopropyl alcohol for 5 min was applied. Additionally, a gold coating was applied via a sputter coating machine (Sputter Coater 108auto, Cressington Scientific Instruments Ltd., Watford, UK) to enhance surface conductivity and improve SEM imaging quality before *in situ* testing. For the *ex situ* case, the coating process was performed after testing to minimize possible modification of the polymer by plasma ultra-violet light emission or the necessary chamber vacuum.

All specimen dimensions were determined via SEM (FIB/SEM 1540 XB, Carl Zeiss AG, Oberkochen, Germany) with 3 kV acceleration voltage pre- or post-testing in the respective cases. As an increase in writing laser power is associated with an increase of the voxel size during printing, every geometry dimension had to be determined individually for the respective laser power levels. For determination of the printed specimen dimensions, each specimen type was printed once, side by side onto a pre-grooved fused silica substrate, which was further split and coated to enable perpendicular imaging and direct measurement of the dimensions of the DENT I part within the SEM [65]. Equally, a full specimen was prepared for the *in situ* experiment. To access the thickness directly under top view, each geometry was printed on a flat substrate and the prints were aborted just above the DENT I part as shown in Fig. 3**(a)** with 45° tilt to visualize the ligament section. All dimensions used for the evaluation can be found in the supplementary Table T1.

For *ex situ* testing, a statistically relevant number of specimens was desired. This is especially uncommon for complex shaped specimens in the field of micromechanics, as considerable fabrication time is commonly involved to produce specimens one by one. But since the specimen manufacturing is automated, only a suitable tradeoff between validity considerations and writing time must be found. For a proper linear regression, as required by the EWF evaluation, 5 ligament lengths were chosen, with 20 specimen repetitions each as a reliable numeric base. So, 20 equivalent specimens of each version (see Fig. 3**(a)**) were printed in two rows, by taking advantage of the scripting option of the TPL system, resulting in a grid of 100 individual PTP devices, as shown in Fig. 3**(b)**, fabricated in one run with equal laser power. For the later surface finding on top of the PTPs during the testing procedure, a simple cube of equal height was added, as well as specimen labels and cross-shaped alignment markers for adjusting the rotation of the substrate towards the axis of the nanoindenter stage. The manufacture of one specimen array as such took roughly 8 h (excluding position and handling time) but chaining of print jobs allowed unattended operation. As the applied methodology yields one value for each whole array, duplicates of equal arrays were manufactured to assess their repeatability. In total, 21 specimen arrays on 3 substrates were fabricated. Supplementary Table T2 shows additional information about printing and testing times, as well as a comprehensive overview of applied parameters.

For accessing the fracture surface area after testing, the effect of local post-curing of the photo resin through e-beam irradiation is utilized as shown in Fig. 4. As the green box (indicated in Fig. 4**(c)**) on one half of the broken DENT I specimen is scanned through imaging under 45° tilt within the SEM, local shrinkage is induced, leading to a strain gradient along the ligament thickness. The resulting bending of about 10-20° towards the irradiated face was sufficient to enable the view on the fracture surface, as shown in Fig. 4**(e)**, where one of the smallest ligament lengths used is depicted for demonstration. One PTP DENT I specimen of every size and writing laser power was selected and subjected to the described procedure to acquire an image of the complete fracture surface and to measure the respective area. A tilt correction to the area is applied afterward.

Since post-mortem determination of the fracture surface area requires this special procedure, just a few specimens can be treated and imaged feasibly. Geometry determination on just a few representative specimens seemed to be sufficient for all equal geometries, as equal objects (obtained by TPL) originated from the exact same print file. Thus, geometrical uncertainties are negligible compared to uncertainties

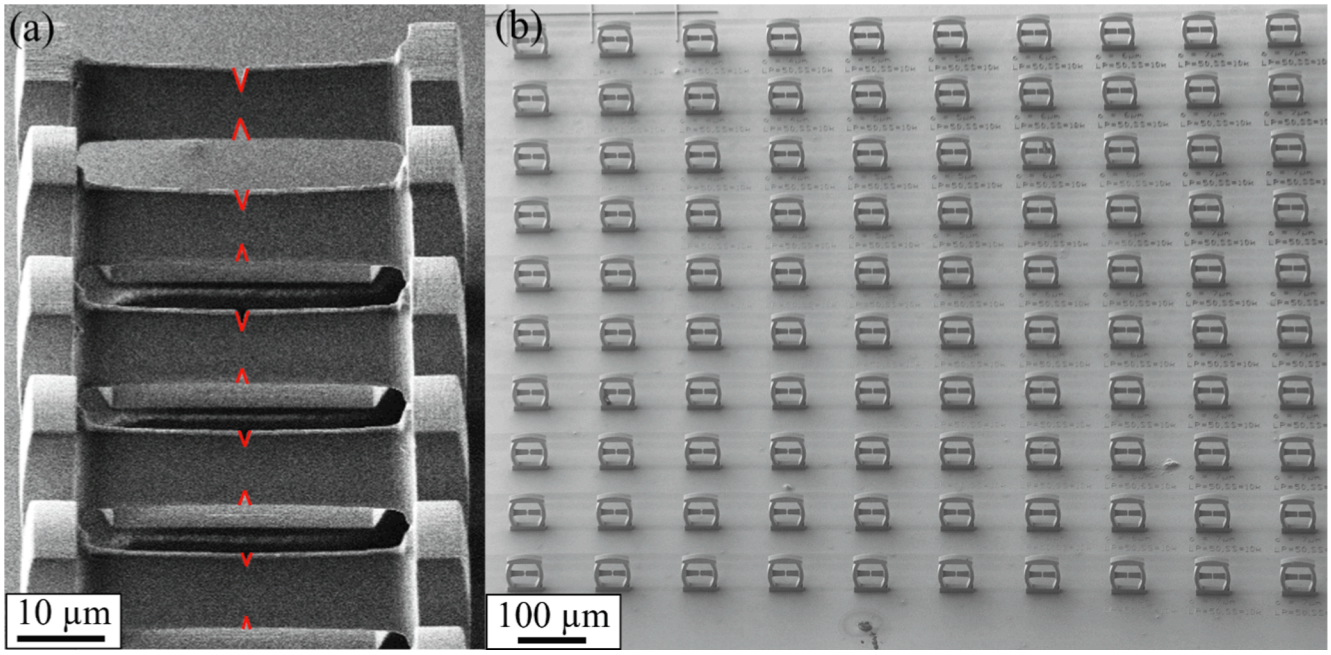

Fig. 3. (a) Overview of all DENT I versions used for the experiments. (b) A SEM micrograph of one PTP-DENT I specimen grid after ex situ testing and gold coating, showing well positioned specimens which could be repeatedly tested via the automated nanoindentation.

of SEM imaging. Major factors of uncertainty are surface charging during e-beam scanning (including possible e-beam shrinkage), visual defining borders on rounded edges (especially if the objects were printing at the resolution limit of the printer) and corrections which must be applied regarding the specimen tilt. Therefore, the finally presented fracture surface areas are mean values over a few surfaces and various image scanning conditions. All obtained data can be found in the supplementary Table T1. The fracture surface areas were used for the EWF evaluation as such, and the ligament lengths were derived from these areas by dividing through the thickness. This way, the deviation from an ideal rectangular shape of the fracture surface was compensated for and a potential misinterpretation of printing-proximity effects within the notch was avoided.

2.3. Compression testing in situ

The *in situ* SEM testing was performed via a displacement controlled nanoindentation system (FT-NMT04, FemtoTools AG, Buchs, Switzerland) within an SEM (LEO 1525, Carl Zeiss AG, Oberkochen, Germany) with a 10 µm circular tungsten carbide flat punch tip and a 200 mN force sensing probe. The loading and unloading were applied with a displacement rate of 100 nm/s in two cycles, where the first one went up to a maximum displacement of 3.3 µm and the second to 4.75 µm. The force acquisition was conducted at 200 Hz and the SEM images (acceleration voltage: 3 kV) were recorded continuously. Force and displacement readings obtained through the testing device were used unaltered.

2.4. Compression testing ex situ

The substrates were glued to an iron disk and mounted onto the sample holder stage of the *ex situ* nanoindenter (TS 77 Select Nanoindenter, Bruker, Eden Prairie, USA) directly after specimen printing. Loading was performed by a self-made diamond flat punch, made by cutting a Berkovich indenter tip (Synton MDP, Nidau, Switzerland) via femtosecond laser processing to be nearly flat [73]. Respective 3D images taken by laser confocal scanning microscopy (LEXT OLS 4100, Olympus Europe SE & Co. KG, Hamburg, Germany) are shown in supplementary Fig. S1. The displacement-controlled loading consisted of two cycles, with a maximum displacement of 3.3 µm, and 4.75 µm on the first and second cycle, respectively. The general displacement rate was varied between 10, 100, 300 and 1000 nm/s, with 1 s hold time at the maximum displacement before unloading. The force and displacement data were obtained directly through the testing device and used as such for the evaluation demonstrated in Fig. 6. The temperature and humidity within the testing chamber were monitored during the experiments and varied slightly between a temperature of 25.1 and 26.6 °C and between 42 and 50% relative humidity.

For the combined testing of a whole PTP specimen field a grid-function was used along the x- and y-axes of the nanoindenter stage, which were aligned manually with the substrate. Starting from one corner, all specimens were tested line-wise and the data were automatically saved afterwards. In general, fracture occurred spontaneously on the first loading cycle before the maximum displacement was reached, producing a drop in force and displacement as the indenter hardware required a certain time to react to the changed compliance. If the load- displacement curve did not show such a distinct force drop (fracture), the individual experiment was regarded as an outlier. Equally, loading curves showing a non-continuous force–displacement curve, caused for example by relative sliding motion between the tip and the PTP specimen, were excluded from further evaluation steps. The second loading step serves for stiffness analysis of the broken PTP.

2.5. Evaluation and data processing

From an experimental viewpoint the EWF scheme enables straightforward calculation of the fracture parameter from the load–displacement curve if dimensions are known. Several hundred files of data can therefore be evaluated automatically via python script (Python 3.8.8). But before the EWF evaluation can be applied a compensation of the individual PTP frame stiffness is required. Firstly, a force of 15 µN was specified as a stable force noise threshold, defining an initial point of contact between the flat punch and the PTP top surface. Secondly, a cubic polynomial with the constant parameter set to zero was applied to the loading portion of the second cycle (after fracture) up to a displacement of 3.5 µm. Finally, the fit was subtracted from the first

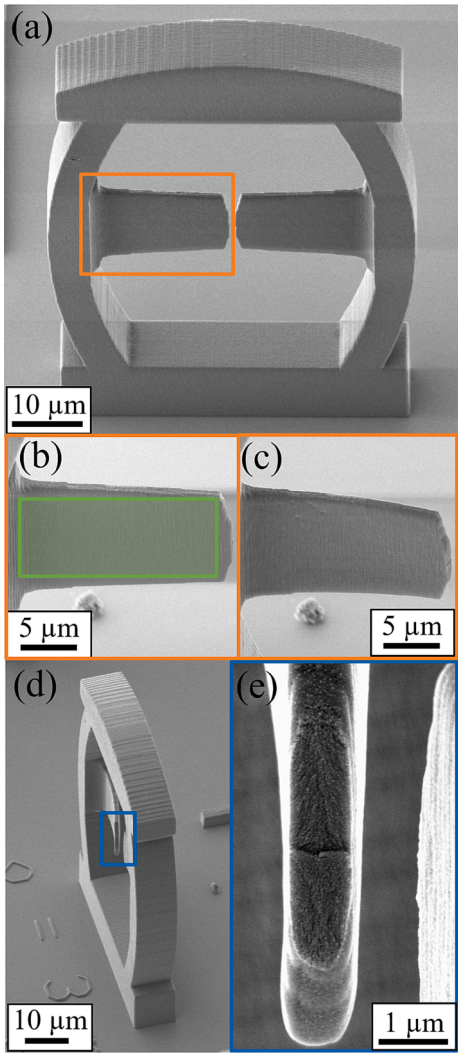

Fig. 4. Illustration of using e-beam post-curing to obtain the area of the fracture surface by bending one half of the DENT I specimen. (a) Post-mortem PTP DENT I specimen with (b) a magnified DENT I section directly after testing. With e-beam scanning (by imaging) at the green marked area for about 5 min, one half of the DENT I specimen is bent out as can be seen in (c) at equal magnification. (d) With suitable microscope stage rotation the fracture surface can be imaged. The blue frame indicates the magnified section in (e). (For interpretation of the references to colour in this figure legend, the reader is referred to the web version of this article.)

cycle to finally obtain the load–displacement curve of the pure individual DENT I specimen without the surrounding PTP frame. On the processed data the force drop corresponding to failure of the specimen was marked and used as an end point for all further processing.

The total work of fracture W_f consists of the essential work of fracture W_e and the non-essential work W_p, as depicted in **equ. (1)** [66]**.** Area specific values can be defined by normalization with the shape of the initial ligament, with l being the ligament length and t the thickness. Since the plastic zone is associated with a volume around the inner fracture process zone, a fracture geometry parameter β is introduced along with the additional dimension of l, which is dependent on the shape of the plastic zone around the ligament.

$$W_f = W_e + W_p = w_e lt + \beta w_p l^2 t \tag{1}$$

For the actual evaluation, the specific work of fracture w_f is plotted against the ligament length l for all specimens tested, to which a linear fit is applied, as shown in **equ. (2)**. The fitting parameters yield the specific essential work of fracture w_e at the y-intercept, and the specific non-essential work of fracture w_p times β, as the slope [74].

$$w_f = \frac{W_f}{lt} = w_e + \beta w_p l \tag{2}$$

According to **equ. (2)**, the total work of fracture W_f was determined by numerical integration up to the point of fracture, and with the associated ligament length l and thickness t, the specific work of fracture w_f was derived. Results of multiple equal specimens are represented as a conventional boxplot, where all data within a single PTP field of approximately 100 measurements give five boxplots with respect to the specimens' ligament length l. Data points outside the higher or lower boxplot whisker (defined by 1.5 times the respective inter quartile range) are counted as outliers and excluded from the subsequent evaluation steps. For the remaining data points, the EWF fit is applied via two standard methods for linear regression to obtain w_e and βw_p, respectively. First, a least-square fitting is applied via an appropriate python library (SciPy, version 1.8.1), and the data are plotted with the Seaborn library (version 0.11.1). A confidence band of 95 % was added to cover the statistical scatter within the data set. Furthermore, 95% confidence intervals for the fitting parameters are derived based on the standard errors of the interception S_{EI} and the slope S_{ES} by **equ. (3) and (4),** where n represents the sample size t_α represents the Student's factor from Student's t-distribution. The latter is a function of the probability level α, which was set to 5% in the current case, and of the number of degrees of freedom, which is $n - 2$.

$$w_{e,1-\alpha} = w_e \pm t_{\alpha,n-2}\frac{S_{EI}}{\sqrt{n}} \tag{3}$$

$$(\beta w_p)_{1-\alpha} = \beta w_p \pm t_{\alpha,n-2}\frac{S_{ES}}{\sqrt{n}} \tag{4}$$

For further calculations, Young's modulus E and yield strength σ_y dependent on the laser writing power and for a strain rate of 1×10^{-3} s^{-1} were considered. For 44 mW an E of 2.6 GPa, as well as a σ_y of 67 MPa was reported at a slightly decreased writing speed of 8 mm/s, together with strain rate and temperature dependency [43]. Another source [40] reported 3.5, 3.7, and 3.8 GPa for E and 72, 75 and 78 MPa for σ_y for the exact same writing speed of 10 µm/s and laser power levels used and based on the degree of conversions (DC) achieved. With 25, 27.5 and 30 mW a DC of about 43%, 44.5% and 46% was estimated, with a maximum DC of about 47% for the used photoresist and system. However, the complex-shaped strain field around the notch is neglected in such discussion, so the authors chose the plain E and σ_y values (3.5, 3.7, 3.8 GPa and 72, 75 and 78 MPa) relative to the applied laser writing power) as baseline values for internal comparison.

The evaluation procedure outlined up to this point was applied equally to all 21 PTP-fields, enabling a comparison of the parameters obtained by the EWF evaluation with regards to laser writing power and testing rate in the following section. For completeness, possible dependencies due to post-curing after fabrication were also investigated, because previous studies revealed a change in mechanical properties such as Young's modulus or hardness within days, even after UV flood exposure [75], or through water uptake [76]. However, as no distinct trends between short (1 day) and long (10 days) times between testing and processing were evident, the results of these experiments are included in the supplementary material Fig. S4, but not discussed in detail here.

The essential work of fracture approach further suggests that the plastic zone radius r_p can be estimated from w_e using **equ. (5)** [74].

$$2r_p = \frac{\pi E w_e}{8\sigma_y^2} \tag{5}$$

It was shown in prior works [77] that the geometry and size independent EWF results are connected to J-integral values. The non-essential work βw_p was related to the tearing modulus of the J_R-curve

and the essential work w_e to the J-integral at critical crack initiation J_i for plane stress conditions. However, slightly higher values might be obtained by EWF [78,79].

2.6. Finite element modelling

The overall influence of the specific PTP sample geometry and printing-related features was addressed in a previous work [65]. Therefore, the new FE modelling stage aimed at determining the influence of experimental misalignment between the nanoindenter tip (which was not ideally flat) with the rounded top section of the PTP samples. This FE model was created and processed with the use of Abaqus (version 2019, Dassault Systèmes, France) code and python scripting (version 2.7.3).

For this purpose, the specimen geometry presented previously (with the DENT I section thickness of 1 μm) was adapted as a baseline geometry imported from the stl 3D model. In order to observe a change in the fracture parameters, a symmetrical crack was introduced in the model, resulting in a ligament size $l = 5$ μm, mimicking the real geometry of the sample with the crack. Since a non-symmetrical positioning of the indenter tip was modelled, the full specimen (without any symmetry plane) had to be modelled. The loading was modelled in two ways: in the first case, as a reference, an ideally flat plane was used to compress the PTP, resulting in reference J-integral and stress intensity factors values. Secondly, a 3D model of the real, non-ideal tip was created as outlined in the supplementary **Figure S1**. Only a minor simplification assuming the symmetry of the tip geometry along the curved edge was used to keep the FE modelling stage within a reasonable time. The model of the non-ideal tip was subsequently positioned in a grid pattern over the top of the PTP by ± 20 μm and ± 10 μm in the length-wise and thickness-wise direction (according to the rectangular PTP base dimensions), respectively, to assess the possible misalignment of the tip with respect to the centre of the PTP. Additionally, since the tip rotation cannot be technically aligned with the stage axis, the rotation of the tip in a range between 0° and 90° in relation to the main PTP axis was considered. For the details on the material model properties, the reader is referred to our previous work [65].

Since the full model would be not fine enough for the precise evaluation of fracture parameters at the crack front, a sub-modelling procedure was used. The deformation field obtained by the global model (meshed with 138,000 3D-stress linear C3D8R elements with reduced integration and using the smallest edge size of 30 nm at the crack tip area and 14 elements through the ligament thickness) was used as a boundary condition for a smaller model, which encompassed only the notched portion of the DENT I part of the PTP. This smaller model could be meshed more finely with pie-like arrangement of the 315,000 3D-stress linear C3D8 elements with full integration and using the smallest edge size of approximately 1 nm at the crack tip area and 30 elements through the ligament thickness.

As results, the J-integral and stress intensity factors calculated with the sub-model and the contour integration method (a built-in feature of Abaqus code) were used and the value for the real tip shape in each position was compared to the results from the ideal planar tip model. To keep consistency between all the results, the values of the J-integral and stress intensity factors for an external loading force of 1 mN were always used.

3. Results

For a general demonstration of the testing procedure, one PTP experiment is presented via SEM *in situ* mechanical testing (see Fig. 5). The standard evaluation is showcased on a representative *ex situ* tested specimen, from which a combination of the results of a whole PTP-field yields an EWF description of the incorporated DENT I specimens (see Fig. 6). Finally, the overall results of 21 specimen fields, covering 1997 equally processed PTP specimens, are shown (see Fig. 7) to demonstrate the high-throughput aspect of the applied methodology and the potential influences of laser writing power during production, as well as of displacement rate during testing, on the EWF of the used photopolymer.

3.1. SEM in situ testing

For demonstration, one specimen was tested within the SEM to observe the fracture event of the DENT I specimen and the deformation of the PTP-frame in detail (see Fig. 5). The load–displacement data are shown in Fig. 5**(a)**, along with corresponding SEM graphs in **(b)** to **(i)** at specific points during the two applied loading cycles.

After establishing contact between the indenter tip and the PTP, the force increases linearly until the first deviation occurs **(b),** quickly followed by crack initiation at point **(c)**. Afterwards, fracture occurs rapidly and only one data point can be captured between **(c)** and **(d)**, where the specimen halves are held in place by the outer PTP-frame. Thereafter, the loading is continued up to the specified tip displacement, followed by unloading until point **(e)**. For capturing the force vs. displacement graph and the stiffness of the PTP-frame, the second loading cycle is applied equally, but up to a higher displacement. Starting from the unloaded PTP device at point **(f),** the displacement on top is transferred to bending of the struts and further to a nearly parallel increase of the gap between the crack flanks at point **(g)**. Near the maximum displacement at point **(h),** a slight rotation of the geometry becomes evident, which is already described in terms of an FE simulation within a previous work [65]. Changes in contrast originate from surface charging with or without indenter tip in contact. Throughout different SEM images (see Fig. 2**(c) and (d)**), this charging pattern changed with respect to viewing angle or scanning conditions, respectively.

3.2. Ex situ testing via nanoindentation

Starting from compression experiments on a single PTP specimen, the evaluation path to finally obtain EWF values from a whole PTP array is presented in Fig. 6. Fig. 6**(a)** shows a raw force vs. displacement graph of one representative PTP experiment. The first loading cycle (indicated by blue bold markers) shows a nearly linear elastic loading section until a maximum is reached, around when crack initiation takes place, followed by a decrease in force corresponding to crack extension. As the used indenter is inherently force controlled for this case, the force-drop at final fracture also results in a jump in displacement until a stable point is recovered again. Following the evaluation procedure as described in the experimental section, and individually shown in Fig. 6**(b),** a force-threshold is applied to redefine the contact point on the second loading cycle and to enable the calculation of the polynomial fit (dashed line). After the subtraction of the polynomial fit from the first cycle, the numerical integral of force over displacement (blue area) up to the point of fracture (last force reading before the jump occurs) can be considered as the total work of fracture W_f. The derived values of specific work of fracture w_f of a whole PTP-array are plotted as statistical boxplots with respect to the ligament length and shown in Fig. 6**(c).** The numbers beside the individual boxplots depict the absolute number of successful experiments, including outliers (round markers). To obtain the essential and non-essential work of fracture, a least-square regression is applied, indicated by the full trendline. Additionally, a 95% confidence band is derived and the y–axis offset as well as the slope errors are determined with a confidence level of 95%. Equivalent graphs of all remaining PTP specimen arrays can be found in the supplementary Figs. S2 and S3.

3.3. Summarized data

In Fig. 7**,** the results of all PTP arrays are shown comprehensively, grouped by applied parameters. In Fig. 7**(a)** the specific essential work of fracture w_e and in Fig. 7**(b)** the non-essential work of fracture βw_p of all DENT I specimen arrays, written with a constant laser power of 25 mW,

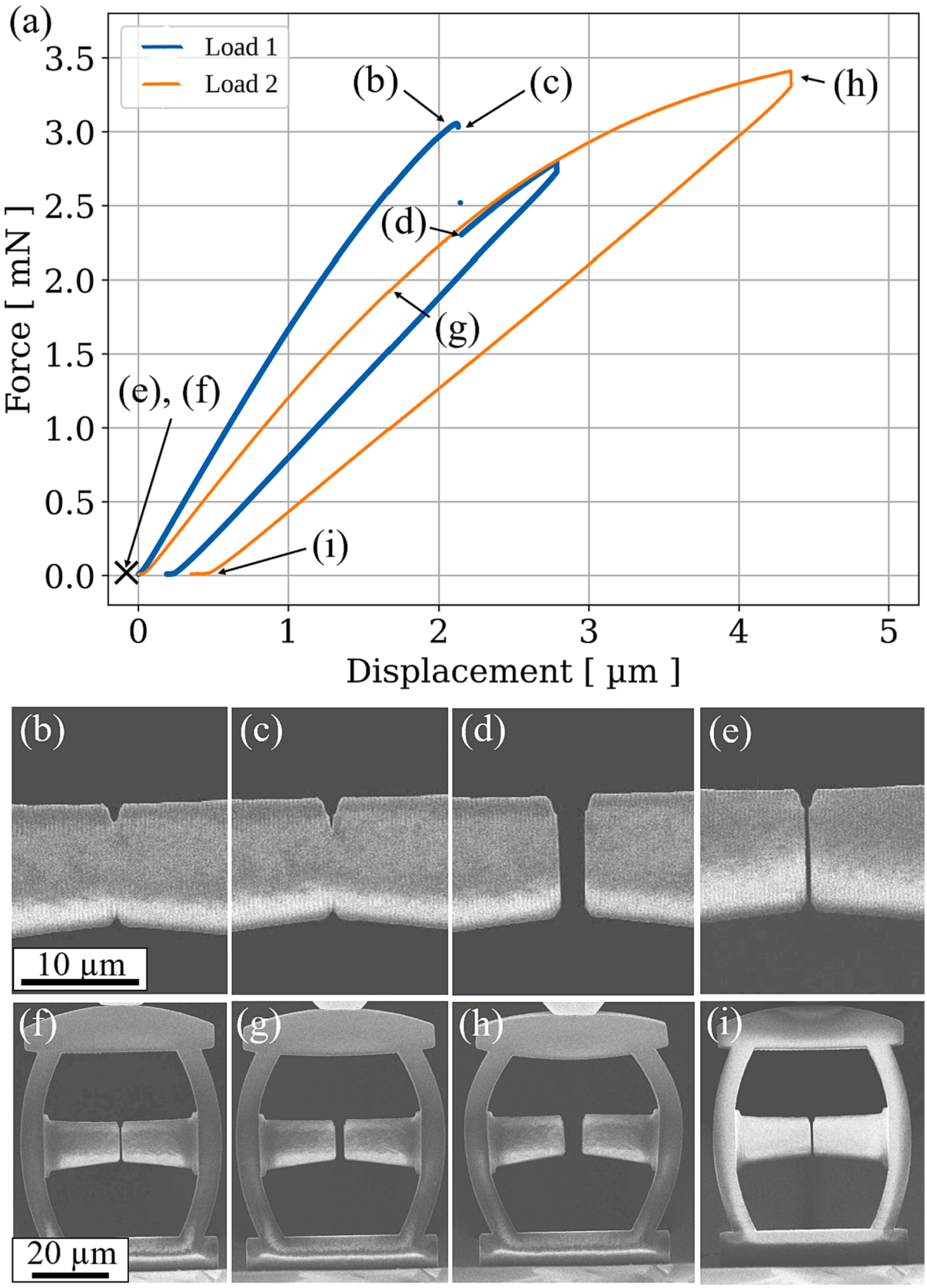

Fig. 5. (a) Force vs. displacement graph of a representative PTP experiment with two loading cycles (first: blue, second: orange). The marked points correspond to the sub-figures (b) before, (c) directly at and (d) directly after the fracture of the incorporated DENT I specimen as well as (e) fully unloaded. On the second loading cycle the response of the PTP-frame is captured, (f) before loading, (g) at about the half the maximum displacement, (h) at maximum displacement and (i) for the fully unloaded state. (For interpretation of the references to colour in this figure legend, the reader is referred to the web version of this article.)

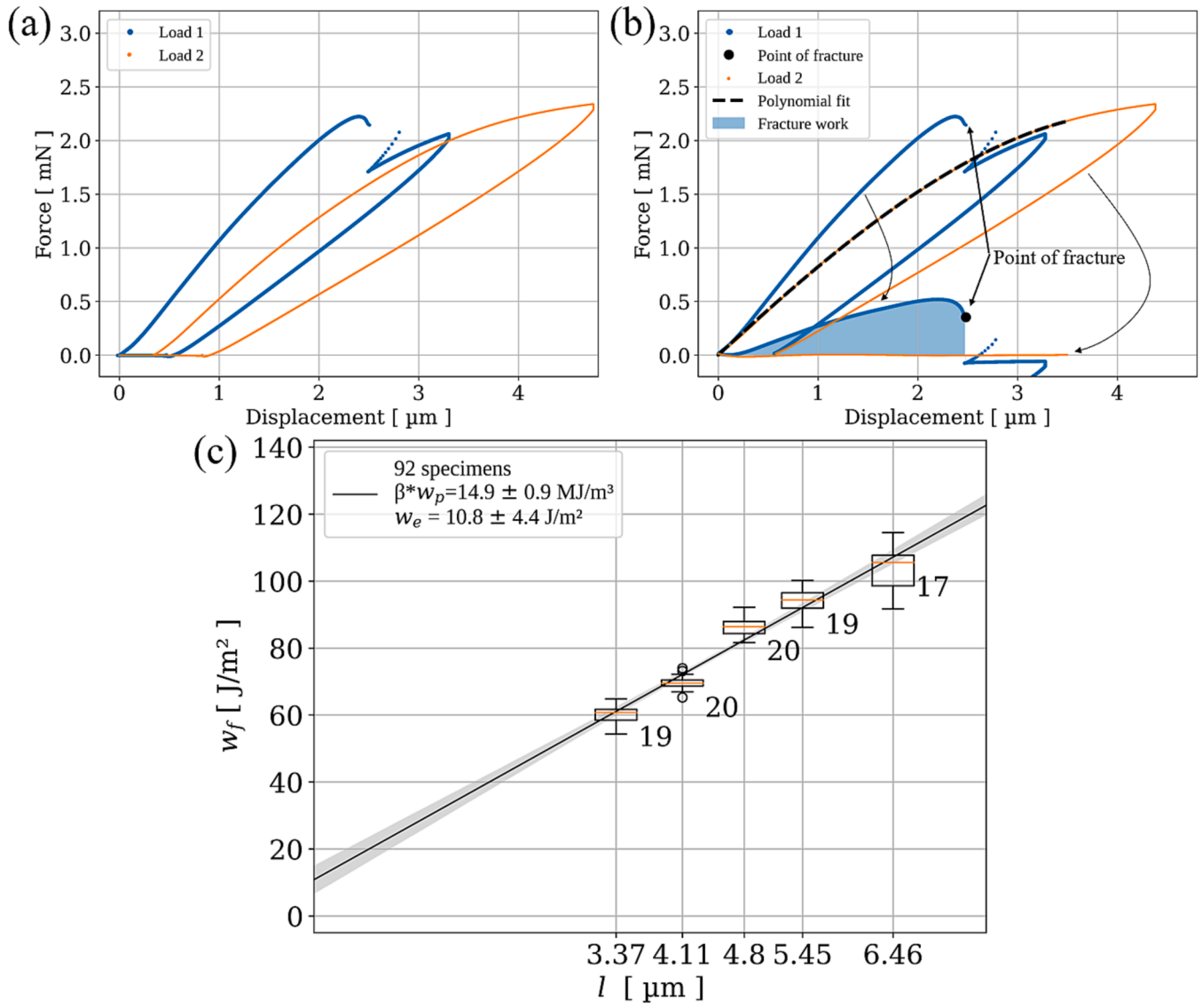

Fig. 6. Representative evaluation and results of one ex situ PTP experiment including (a) initial load- displacement curve of the first and second loading cycle, (b) offset data with polynomial fit (applied to the second loading cycle) to be subtracted from the first loading cycle and thereby obtaining the data of the pure DENT I specimen. Integration until the point of fracture (shaded area) yields the total work of fracture W_f. (c) Summarized results of derived specific work of fracture w_f values of 100 PTP DENT I specimens containing grid (excluding 8 outliers). Specimens of equal ligament length l are depicted as boxplots (number indicated included entities). The black line shows the EWF regression (least-square method) applied, including 95% confidence band (light grey region).

but tested with varying displacement rates are shown. In Fig. 7**(c) and (d)** the EWF evaluations for PTP-arrays tested with constant displacement rate, but written with different laser power, are shown, respectively. Data for 25 mW and 100 nm/s are included redundantly. For summarizing the results, inverse variance weighted average values were calculated, but datapoints with strongly negative mean values (below −10 J/m^2) were omitted due to their unphysical characteristic. Possible reasons for obtaining negative w_e will be discussed later in detail. The weighted average value of w_e, obtained with laser writing power of 25 mW, yields −1.5, 8.5, 8.2 and 12.1 J/m^2 for 10, 100, 300 and 1000 nm/s displacement rate, respectively. For βw_p and equal displacement rates, the values 14.7, 14.3, 15.2 and 15.6 MJ/m^2 were obtained. Regarding writing laser powers of 25, 27.5 and 30 mW, w_e values of 8.5, 7.6 and 26.3 J/m^2 and βw_p of 14.3, 10.1 and 10.6 MJ/m^2 were obtained, respectively. Based on the shown data, only a very weak correlation between testing displacement rate and w_e or βw_p seems to be present, buried within the scatter between separate measurements. Further, the w_e values show a slightly increasing trend towards highest writing laser power.

3.4. FE modelling

Since no direct information about the local rotation of the indenter tip or contact point position between the real flat punch and specimen shapes exists, FE simulations were carried out with different tip rotations and positioning, as shown in schematically in Fig. 8. The contour plots show the relative calculated *J*-integral values on the uncracked ligament with respect to a perfectly flat and centred contact. Each plot corresponds to a 30° increment of tip rotation and the individual *x* and *z* correspond to the lateral offset between specimen- and tip centres.

For the case of physical experiments, the actual tip rotation is unspecified, but will not change during the experimental session, which is not the case for the lateral offsets. As relative positioning errors are present during stage movements upon fabrication and testing, the exact point of contact will change within the positioning precision, which is on the order of 10 µm as a rough estimation over about 1 mm travel within the PTP field. However, the simulation can rationalize the magnitude of misorientation error, which seems to lie within 10% for most of the cases. It should be noted that due to the use of one symmetry plane of the

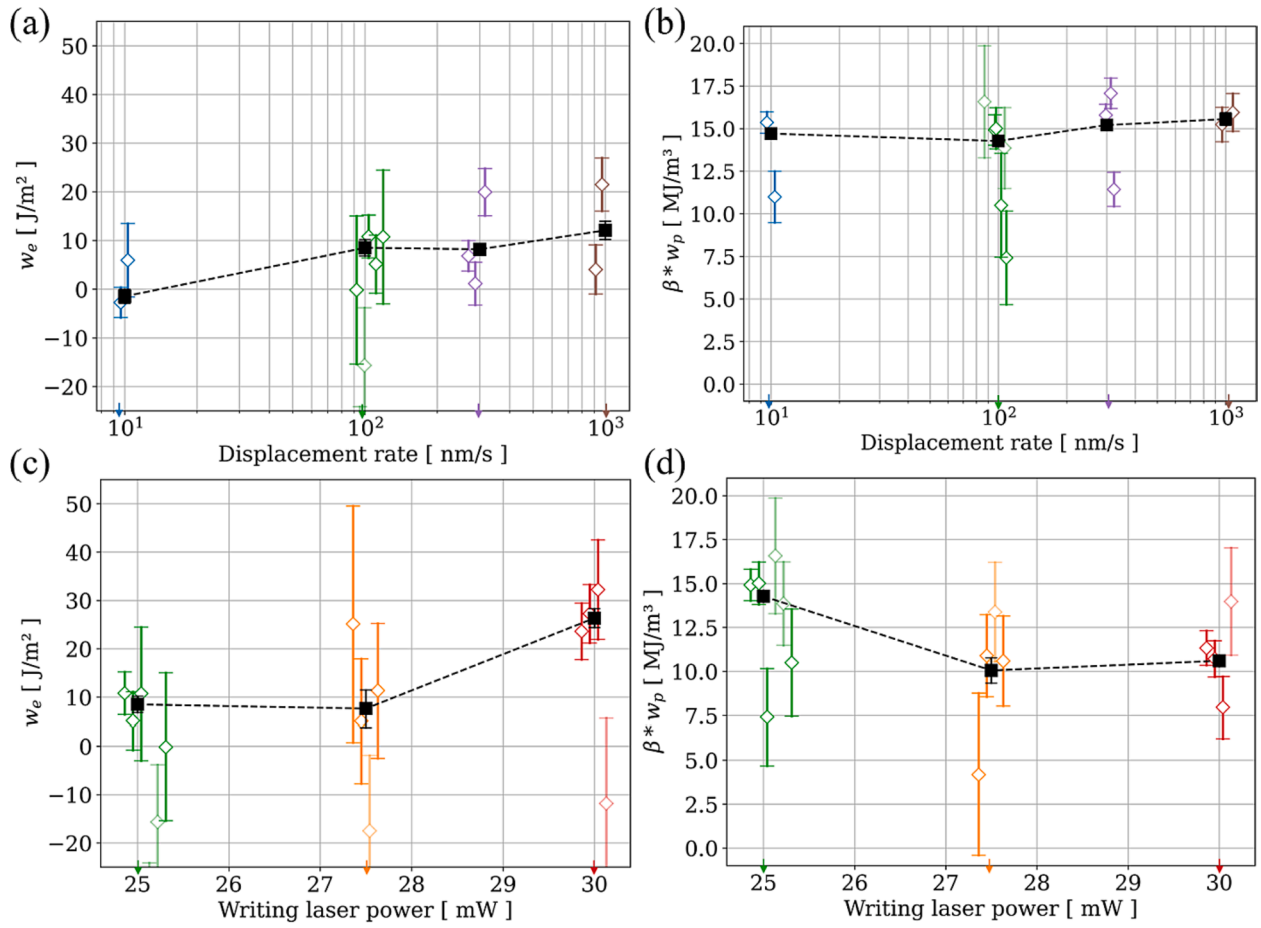

Fig. 7. Comprehensive summary of parameters obtained from regression of all 21 EWF fits (1997 single PTP DENT I specimens) including 95% confidence intervals as error-bars. For better readability, random spacings were introduced between discrete dimensions on the x-axis. (a) The specific essential work w_e and (b) non-essential work of fracture βw_p plotted against the individually applied displacement rate during testing (10, 100, 300 and 1000 nm/s), of specimen arrays processed with constant laser power (25 mW). Similarly, (c) and (d) depict results with respect to different laser writing power (25, 27.5 and 30 mW), but at constant loading displacement rate (100 nm/s). Variance weighted mean values are depicted with black markers, connected by a dashed line. Data points with strongly negative w_e values (below -10 J/m^2) were excluded before averaging (indicated by transparent symbols).

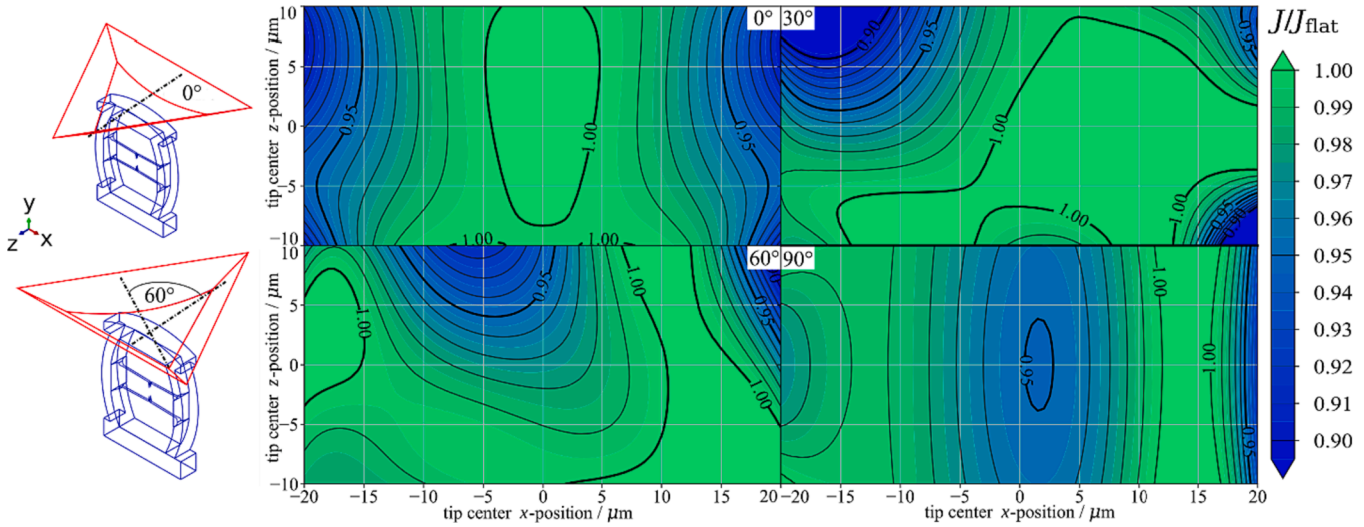

Fig. 8. Relative acting J-integral value at the notch tip (at 1 mN load) for loading through the real flat punch tip normalized by the value for an ideally flat contact, with respect to x- and y-offset and discrete tip rotation (indicated by the white box in every subplot). Every contour plot depicts a different 30° indenter rotation increment, while the corresponding 3D views on the left side showcase the simulated geometric state for 0° and 60°.

tip model, the resulting contour plots for 0° and 90° tip rotations are symmetrical along the $x = 0$ μm and $z = 0$ μm lines, respectively. The real, slightly unsymmetrical tip can, on the other hand, introduce small asymmetry in such results. However, since the tip shape asymmetry is almost negligible, the deviation of the results would be negligible as well. Additionally, due to the symmetry of the PTP specimen, only the cases of 0° to 90°, with 30° increments in tip rotation, were modeled and presented.

4. Discussion

4.1. PTP methodology and parameter influence

For demonstrating the high throughput nature, versatility and straightforward application of the presented method, specimens were manufactured and tested with two significant experimental parameter variations. The laser writing power corresponds to the intensity of light used during specimen fabrication and therefore increases the crosslink-density with increasing writing power. This subsequently results in a change of mechanical response, as both the yield onset and the Young's modulus increase with increasing laser processing power [40]. Thus, an increase of w_e with laser writing power parameter (see Fig. 7**(c)**) is plausible.

Young's modulus and yield strength are also intrinsically influenced by the applied strain rate, as common for polymer type materials [43]. Up to this point, all results were presented as a function of the displacement rate of the indenter tip on top of the PTP-frame, and not directly as a function of the strain rate of the DENT I specimen. Starting from the assumption that only elastic deformation occurs along the PTP-frame, energy conservation would suggest that the strain rate is constant over the frame, and only changes at plastically deformed regions located near the notch for the present case. The translation of displacement to strain through the PTP-frame to the DENT I is less straightforward. For a direct approach, traceable features on the specimen could be added, which would allow visual determination of the displacement shift and subsequent calculation of the strain. This is a common approach in small-scale testing, where the displacement cannot be accessed directly [80–82]. For an even more advanced case, digital image correlation could be employed to track specific surface features over the whole ligament and thus obtain a 2D strain map for every imaging step. This approach could be very promising for future works, as such features could be easily added to the printed specimen. For estimation of 3D strain information, shape correlated FE simulations could be employed, even capturing the strain rate field around the notch with high precision.

However, for the present work, a first order direct observation of displacement on top of the PTP-frame and crack opening in the DENT I region was performed by manually tracking the decrease of the crack flank distance during unloading in *in situ* experiments (see Fig. 5). A relation between crack flank closing and retraction displacement was measured, suggesting a direct translation of displacement on top of the specimen and crack opening. Consequently, the testing displacement rate on top of the PTP-frame gives a good estimation of the local displacement rate of the DENT I specimen, considering initial linear elastic assumptions. With a 38 μm long DENT I specimen, the engineering strain rate is roughly between 3×10^{-4} s^{-1} for 10 nm/s and 3×10^{-2} s^{-1} for 1000 nm/s.

Obviously, experiments within selected PTP arrays show some scattering. The total work of fracture values scatter within a group of equal specimens or within the whole array (see Figs. S2 and S3), although unreasonable load–displacement data (as cause by out of plane bending or slipping) were already excluded in the evaluation routine. The inconsistent load vs. displacement behavior might be also related to the displacement shift between the first and second loading cycle (see Fig. 6**(a)**). After offsetting the load–displacement curves of the first and second loading cycle (see Fig. 6**(b)**), overlapping regions underline the assumption that no significant yielding of the PTP-frame occurred up to the maximum displacement of the first loading cycle. Therefore, the non-linearity is reproducible to a large extent and is therefore assumed to be visco-elastic and thus recoverable. If not considered, the non-constant shift of the contact point would lead to over- or underestimation of the total work of fracture after subtraction of the values obtained by the PTP-frame-compliance fit and introduction of scatter. For a few experiments where the time between first and second loading cycle was increased (*in situ* SEM experiment) this systematic offset towards a slightly higher displacement was less pronounced or even diminished entirely. This leads to the assumption that incompletely recovered visco-elastic deformation might be the origin. Detailed investigations of the influence of visco-elastic contributions will be the focus of future work.

The lateral offset is mainly determined by the manual positioning via the nanoindenter optics on the first PTP specimen (as further positions are pre-programed) and with slight imprecision due to the resolution levels of the stage controls of the indenter and TPL-printer. Slight unavoidable clearance in the printer and indenter stage might therefore influence the testing results systematically, as the position misalignment could sum up. The imperfect rounded shape of the indenter tip is likely to enhance this issue, as position dependent errors are introduced. Furthermore, the nanoindenter's optical magnification is fixed, limiting the initial optic-to-tip calibration accuracy to the order of micrometers. With FE modeling and simulation, the effect of actual indenter shape and misorientation errors along testing can be captured, as detailed in Fig. 8. The simulations showed a maximum J-integral decrease in the range of 10%, when ideal and non-ideal tip at various positions and rotations are compared for the same load level.

Although the introduced error changes the stresses at the crack front for the same loading level, it is not affecting the work of fracture evaluation used in the results assessment. The different position and contact between the tip and PTP have an effect not only on the J-integral value, but also on the overall PTP stiffness response. Both phenomena are embedded in the measured load–displacement curves, resulting in a theoretically unchanged area beneath the curve until the point of fracture, since the work of fracture depends only on the material itself and the loading regime, which did not change with tip misalignment. Therefore, the change in J-integral associated with the tip misalignment can be considered to have negligible impact on the experimental results as long as the tip remains in rigid contact with the PTP during testing. This supports the validity of the measurements and suggests that the spread of total work of fracture W_f amongst the individual experiments with equal geometry is material inherent stochasticity, at least to a large extent. Another origin of scatter might be introduced by the relative change in stiffness and shape of the PTP between the first and second loading cycle, caused by the positioning of the contact between the tip and PTP. If the PTP's top is not met centrically, the simulations showed slight non-symmetrical motion of the PTP, leading to a significant reduction in stiffness due to uniform sidewise bending instead of symmetric outward bending of the PTP's struts. It can be argued that if the deformation of the PTP is generally elastic, the contact point should stay unchanged between the first and second loading cycle, and therefore, the relative stiffness should be comparable. Nevertheless, some experimental uncertainties (e.g. printing artifacts or local compaction under the indenter tip), can lead to slight deviations between first and second load segments. After offsetting of the load–displacement curves (see methods section) during the experiment evaluations, this change in stiffness can lead to a stochastic error at subtraction of the fits. Therefore, it was found to be important that the subtraction of the second loading cycle be part of each experiment individually, as a global 'mastercurve' would yield an increased uncertainty with regards to the W_f values.

Furthermore, an off-centric loading of the specimen might lead to mode II or mode III stress intensity contributions. These would lead to misinterpretation of the experimental results obtained, since crack resistance values are strongly dependent on the mode and pure mode I is assumed [83]. These contributions were investigated in the already

presented FE simulations and can be found in supplementary Figs. S5 and S6. There, the corresponding normalized mode II and mode III contributions do not exceed 1%, independent of rotational and positional misalignment. Therefore, the present PTP geometry can be considered to obtain pure mode I results with reasonable accuracy.

While future experiments should strive for a flat indenter tip to avoid potential errors and FE simulations, the resulting low standard deviations on a significant number of experiments as well as the supporting FE simulations and arguments outlined above suggest the validity of the presented results, even with the non-ideal indenter tip geometry.

As the indenter tip, the specimen shows deviation from the ideal shape. Fig. 2 shows a direct comparison of ideal and printed DENT I geometry to visualize geometry imperfections. Discretization errors lead to rounded edges and local deviations between designed and realistic geometry, followed by inherent shrinkage during development. Thus, the exact specimen dimensions must be determined after fabrication, especially if object dimensions are near the resolution limit of the two-photon lithography device. Besides the mentioned dimension (see supplementary Table T1), a notch radius of 200–400 nm was achieved directly by laser writing. Since further post-processing steps are avoided, any damage to the material is avoided prior to testing. Thus, no effects of artificially introduced notches (as by cutting or ion milling) will affect the EWF values [84]. The present notch-tip presumably shows a larger radius than a natural pre-crack tip. Therefore, the presented values might be influenced by the notch radius and not only by the materials resistance against crack initiation. A smaller opening angle might lead to sharper notches but might also lead to proximity effects near the notch, meaning imperfect polymerization. An in-depth investigation on achievable notch radii will be the focus of future works and should lead to ascertaining the ideal parameters for achieving the sharpest possible notches. This is important as blunt initial notches result in systematically higher EWF values [85].

Another source of error is the uncontrolled post-curing (associated with shrinkage) of the photopolymer by UV-light or e-beam irradiation. UV-irradiation is avoided by not exposing the samples to sunlight prior to testing, so the material properties should not be changed. However, a certain amount of post-exposure [75,86] could take place after testing within the gold sputtering device, as the specimens are exposed to plasma for applying a conductive gold layer for SEM imaging. This procedure does not influence the experiments directly but is required to obtain the specimen dimensions from SEM images. If uncoated, charge accumulation of the electrically insulating polymer and substrate would lead to considerable image distortions during build-up.

During imaging, even with a low acceleration voltage, a sink-in of these regions takes place due to post-curing directly by electron irradiation or by the introduction of local heat. Also, post-curing due to e-beam irradiation was reduced to a minimum by limiting the imaging time (and use of fast scanning modes). Otherwise, this effect was used beneficially to deform certain printed regions. By irradiating (through extended imaging) the DENT I specimen one side is bent purposely sidewards, enabling to image the fracture surface, as indicated in Fig. 4.

For estimating the effect of residual stress (due to shrinkage by the TPL process) on the w_e, a separate experiment was conducted, whereby the details are outlined in the supplementary material. To our concern, the EWF results would have to be shifted by 0.39, 0.22, or 0.10 J/m^2 for the respective laser writing power (25, 27.5 or 30 mW). Therefore, the influence of residual stresses lies within experimental and fitting uncertainties and can be safely neglected for the given specimens.

Despite these TPL associated peculiarities, one should not oversee the main aspect of relative position accuracy enabling reproducible specimen manufacturing, which enables high throughput testing in the first place. Regarding overall testing time, the time spent for initial alignment and setting up the indentation methods at the specified positions (together just a few minutes), which must be performed once per substrate, can be neglected since one substrate bore multiple arrays. The loading rate remained the most significant time factor – single experiment took from 17 s (for 1000 nm/s displacement rate) up to 28 min for the 10 nm/s displacement rate. Thermal drift correction was performed on top of each specimen for the individual experiment via the standard approach consuming additionally about 40 s. Since the stage movements are limited to repositioning and a minimum retraction can be chosen between single experiments, just a few seconds are added, depending on the traveling path. Altogether, testing of one specimen array with the "standard" loading rate of 100 nm/s took roughly 8 h, which is not optimal. Besides minor adjustments, the unloading rate could be increased considerably as no data are used from this section with the present evaluation procedure.

In principle, the methodology is not limited to small-scale specimens and might be employed for *meso*-scale or large-scale 3D manufactured materials. However, as larger scale specimens allows for easier handling and easier achievability of size restrictions for standardized sample geometries the key advantage of the such push-to-pull type geometries might not be as prevalent as for micron sized specimens. Furthermore, the easy accessibility of precise nanoindentation device which allows for automated testing of a very high number of specimens (on a micrometer scale), while mm sized specimens might necessitate a custom solution compression testing rig. Still all the benefits of 'theta'-specimens in comparison to common tensile type specimens (misalignment issues, specimen mounting) hold independent of size and might lead to easily accessible statistically significant evaluations on any scale.

4.2. EWF – General considerations

As for the standardized method, validity considerations should be carefully discussed on the miniaturized version. The fracture behavior of the *in situ* specimen suggested brittle failure with no directly visible signs of plastic deformation. This is evident on the fracture surface depicted in Fig. 4**(e),** where smooth surfaces on top and bottom of the image indicate prior notch regions until the surface impression change towards the actual fracture surface closer to the ligament center. Crack marks describe a crack originating from the center of both notches stretching towards the remaining ligament thickness with an equal surface impression through the whole ligament thickness. As the cracks do not meet at the very same position, a visible surface step developed slightly nearer towards the lower notch. These more or less pronounced steps at individual specimens might originate from a slightly off-centric loading on top of the PTP-frame, influencing the crack direction to a small extent. All features described are common for brittle failure. Fracture surfaces show no change in appearance irrespective of ligament sizes. Furthermore, similarity of the load–displacement curves (after compensation of the PTP-frame) indicates no change in failure mode across different specimen geometries.

A generally stable crack growth is evident at crack initiation, from images captured in this phase and the section of decreasing force after the maximum force is reached (see Fig. 6 **(a) and (b)**). It should be mentioned that the indenter for the *ex situ* experiments is inherently force-controlled, which is unfavorable for stable crack growth. A full yielding of the ligament, as required by the EWF method, cannot be confirmed visually (as crazes on larger specimens) before the crack propagates. Furthermore, the *in situ* SEM experiment indicates unstable (spontaneous) crack propagation after the initially stable onset.

Exact size requirements, as developed for standard size specimens, are still scientifically discussed in the light of the present small-scale experiments. A lower boundary of the ligament length $l > 3\text{-}5\ t$ was established [70,74] (with t being the specimen thickness), which is the range of the smallest ligaments produced within the present work. Thus, this requirement is fulfilled at least in the less restrictive version ($l > 3\ t$) in every case. Hashemi [87] argued, that $l > 5\ t$ would be required for pure plane stress conditions (especially for polymeric materials), but that mixed mode cracking, as if the ligament size surpasses the plastic zone, would not affect the linearity of w_f vs. l trend considerably [68]. However, some literature data well below the $l > 5\ t$ border also leads to

a deviating slope, suggesting that the strict thickness and ligament independence of w_e does not hold anymore for an increasing plane strain state [88–90]. Otherwise, it was suggested to find the loss of linearity based on a statistical approach presented in [91]. The upper boundary of $l < W/3$, with W being the unnotched specimen width, could be not fulfilled with the current specimen design. However, as trying to fit all the different ligament lengths between these restrictive bounds would lead to very small spacings between them, the limited linear extrapolation range would lead to considerably larger uncertainties. Therefore, it was decided to utilize the larger spread of ligament lengths, neglecting the upper bound criterion.

Another interpretation requires $l < 2r_p$ (see **equ. (3)**) to ensure full yielding of the ligament. If the plastic zone radius is estimated for the size regime of the presented results (meaning a w_e of around 10 J/m^2 and with above mentioned material parameters), $2r_p$ yields 2.8 μm, which is smaller than all ligaments used. Duan *et al.* [92] modified the EWF model to capture the effect of fully developed plastic zone, which does not fully cover the whole ligament, leading to bi-linear w_f vs. l correlation. As no such trend was observed in the present data, the results are considered to lie within the regime of the initial linear description of the EWF methodology.

Another recommended approach is to test for Hill's plasticity criterion [93] and a plane stress state, as required by the concept of EWF measurements. Therefore, the cross-sectional net stress σ_N at maximum force ($\sigma_N = F_{max} / (lt)$) should be smaller than 1.15 of the yield strength. If this is not the case, a mixed mode stress state is present for elastic-perfectly plastic materials [78]. For strain hardening materials, the ultimate tensile strength should be used instead of the yield strength [94]. To visualize Hill's plasticity criterion for the present case, suitable plots were added within the supplementary material (Fig. S3), where the maximum force after compensation for the PTP-frame was used as F_{max}. In every case the criterion is fulfilled just nearly or not at all. It should be underlined that the tensile yield strength should be taken as an estimate due to the small number of references for IP-DIP, and that the overall strain rate used for estimating the yield strength is based on a second assumption, namely neglecting the influence of the notch. With a strain rate of about 3×10^{-2} s^{-1}, which is near the applied value, the yield strength of IP-DIP surpasses 100 MPa [43], at which a considerable amount of specimens would fulfill the Hill's plasticity criterion. Another empirically found criterion suggests that σ_N should not deviate>10% from the mean value to ensure an equal stress state within all specimens. This criterion is never fully fulfilled, as the ratio of specimens outside these borders varies between 7% and 94% for the PTP arrays presented. An indirect determination of F_{max} based on the frame stiffness compensation is the most likely origin of this deviation [95].

To summarize, exact determination of valid ligament lengths is not possible, as the stress state cannot be directly accessed. The transition between pure plane stress and plane strain dominated geometry dimensions is uncertain, with mixed stress state present in between. The authors of a recent work suggest finding the upper dimensional limits (l, t) via digital image correlation. The lower limits could be accessed via the loss of linearity, on which the EWF approach is founded, and indicating the presence of a mixed stress state [91], backed with FE simulations in the optimal case [96]. If the borders could be found with high certainty, the work suggested distributing the specimens at targeted points to control the variance of EWF results or optimizing the specimen material [97]. A general comparison to macroscopically sized EWF values cannot be performed straight forward, since as the fracture toughness is inherently sheet thickness dependent in plane stress conditions.

A negative specific essential work of fracture w_e, would indicate a negative binding force within the solid, which is unphysical as at least the surface energy is required to force a crack through a bulk solid. As the specific essential work of fracture w_e is a result obtained by linear extrapolation, the value is significantly influenced by relative changes of the data point spacing used for fitting or other experimental uncertainties, which might have summed up to finally negative values in extreme cases. Otherwise, taken as such, negative results for w_e might be a hint for a change in stress state during loading [71]. However, the majority of the data shows a linear trend with physically reasonable scatter, and an evident linear trend suggests a significant content of plane stress state. The measured absolute values for w_e of 7.6 – 26.3 J/m^2 seem comparable with chemically similar material values form filled dental resins (11 – 47 J/m^2, derived using plane stress assumptions [98] with Young's modulus of roughly 6 GPa for the respective composites [99,100]) [101]. Thus, the obtained values do not seem to be unphysical, although they are low in general.

While Young's modulus and yield strength of IP-DIP increases by 20% to 54%, within the range of tested strain rates [43], a nearly constant w_e is present, rendering the behavior a nearly rate independent. With respect to potential loading rate effects [102], the displacement rate was varied over three orders or magnitude and no clear trend of w_e was observed, which could be due to several reasons. Since the displacement rate could be only derived from the indenter tip and not measured directly on the specimen, the applied displacement rate might not be directly translated within the PTP-frame due to some viscoelastic relaxation in principle. Other studies reported a small decrease of the fracture toughness (from 0.95 to 0.8 MPam$^{0.5}$) with increasing crack tip strain rate (1×10^{-4} to 0.1 s^{-1}), associated with change of crazing behaviour [103].

4.3. EWF vs. Linear elastic description

As the *in situ* experiment (Fig. 5**(c)**) depicts, stable crack growth is only evident for a small portion of the load–displacement curve, and is followed by rapid crack extension. This behaviour is not identical to the standard EWF measurements where a continuous decrease in load down to zero is commonly observed. Therefore, a complete plastification of the present specimens is not inherently evident and it can be argued that the fracture process could, to a certain extent, be governed by stress intensity, *i.e.* linear elastic fracture mechanics considerations. The groundwork for linear elastic analysis within the present specimen has already been described in an earlier work [65]. Abdellah *et al.* [104] showed recent experimental results on semi-brittle fiber-reinforced epoxy specimens, where classical stress intensity (K_I) measurements were compared with results obtained from EWF and extended FE approaches and found that even in the case of semi-brittle behavior, the EWF methodology seems to remain valid. For avoiding misinterpretation, the diametrical difference between the fully plastic and energy-based EWF and the linear-elastic stress intensity based K approach should be underlined at this stage. As the principal models rely on different fundamental assumptions translation between values, even for comparison, should be performed with great awareness of mixing different concepts. Valid unconditional critical fracture toughness values (J_{IC} / K_{IC}) can be obtained only within the borders of standardized testing methods and validity criteria, presumably requiring larger dimensions of specimens on the current material.

Therefore, a comprehensive comparison of current results within the frameworks of EWF and linear elastic analysis is given in the following. The required geometry factor for the entire specimen geometry was originally derived for the purpose of (linear elastic) FE simulation, which is now used with experimental data. The maximum force of the individual PTP experiments has been found to correspond to the crack initiation point during the *in situ* experiments, and a conditional stress intensity factor for mode I fracture, K_{FE}, near to the crack initiation value can be estimated via the previously derived geometry function.

Only for comparison of linear elastic and essential work of fracture concepts, the relation $w_e \triangleq J_i$, which is valid for the DENT I specimen geometry [77,88,105] is employed to derive a stress-intensity-based fracture quantity for crack initiation K_{we}. Therefore, Shih's general relation for plain stress condition, shown in **equ. (6)** [98] is used [77].

$$w_e = \hat{} J_i = \frac{K_i^2}{E} \quad (6)$$

Consequently, the results can be compared as depicted in Fig. 9**(a)**. There, the linear regression was equally applied to the w_f trend as described in the experimental section, with its results in the legend. As K_{FE} values are not expected to show any trend with l, a mean value over all results of the PTP array, $K_{Q,\ FE}$, is calculated and represented as dashed line with two standard deviations (corresponding to a 95% confidence band) as a measure of uncertainty in grey in Fig. 9**(a).** A slightly increasing trend with l (depicted by the lower slope triangle) is neglected, which suggests a far field stress (T-stress) influence of the specimens in the chosen ligament range, where the shorter ligament lengths already exhibit the influence of a plane strain contribution, *i.e.* a lower apparent fracture toughness in comparison to the longer ligament lengths [91].

Even with the difference between the two analysis variants and by neglecting some restrictions in a classical fracture mechanical sense it is evident that both methods lead to comparable results as their intersection at $l = 0$ µm is in good agreement. This suggests that the EWF methodology is also applicable for determining w_e within quasi-brittle fracture characteristics on the microscale as has also been observed previously on macroscopic fibre reinforced laminate specimens [104].

This dual analysis has been conducted for all PTP arrays in this work and the results are shown in Fig. 9**(b)**, where all derived K_{we} are plotted against $K_{Q,\ FE}$ with corresponding uncertainties. The markers indicate the laser power levels applied for specimen processing as indicated in Fig. 7, but not differentiated with respect to displacement rate applied. Negative and non-physical K values were omitted. While qualitatively, the average of all data points seems to show a 1:1 correlation, it is evident that the values obtained via EWF show a significantly higher scatter when compared to the linear elastic values. However, with respect to experimental evaluation of future materials, which might exhibit stronger non-linear elastic behaviour the EWF method remains promising, as it is less influenced of such processes.

5. Conclusion and outlook

Within this work, a methodological approach for fracture analysis is presented. It includes specimen fabrication, mechanical testing, and evaluation – all tuned for small-scale specimen testing in a high throughput manner. This work showcases high throughput testing of over 2000 complex shaped specimens on the micrometre scale, presenting the possibility of testing specimens produced by TPL and obtaining statistically significant data. A printed PTP geometry incorporating a DENT I specimen is used and automated mechanical testing is realized by a nanoindenter. Furthermore, an EWF evaluation scheme was detailed and applied to study influence of displacement rate and TPL laser power on fracture parameters. For the negative tone TPL photoresist IP-DIP, a specific essential work of fracture w_e between 7.6 and 26.3 J/m^2 and a non-essential work βw_p between 10.1 and 15.6 MJ/m^2 were determined. The EWF parameters reveal a negligible influence of the displacement, strain rate or ageing time, but a slight increase of w_e with laser writing power.

By combining the presented methodology with additional specimen geometries such as micro-pillars, material properties (such as E and σ_y) of photoresists might be determined within one automated experimental session. Furthermore, the use of such base specimens in conjunction with thin film deposition techniques would facilitate investigation a variety of material combinations. From that, a standardized testing procedure could be formulated, including a list of scalable digital specimen models arranged side by side and uniformly manufactured. As the global actuation remains limited to compression testing, and therefore avoids individual complex positioning efforts, automated testing on a statistically relevant number of specimens can be performed in a straightforward manner. With the inclusion of additional calibration bodies, where important dimensions are directly visible (such as PTP devices without the top part printed), the determination of under- or oversized geometries by the printing process could be reduced to a minimum.

Given the relevance of TPL photoresist material systems in several rapidly growing fields, such as flexible electronics, microfluidic lab-on-a-chip, smart textiles, and the need for a reliable design, we hope that this testing concept will facilitate valuable insights into various materials science problems in the future.

CRediT authorship contribution statement

Alexander Jelinek: Software, Investigation, Writing – original draft, Visualization. **Stanislav Zak:** Formal analysis, Writing – review & editing. **Megan J. Cordill:** Resources, Writing – review & editing. **Daniel Kiener:** Resources, Writing – review & editing, Supervision, Funding acquisition. **Markus Alfreider:** Conceptualization, Methodology, Formal analysis, Writing – review & editing, Supervision.

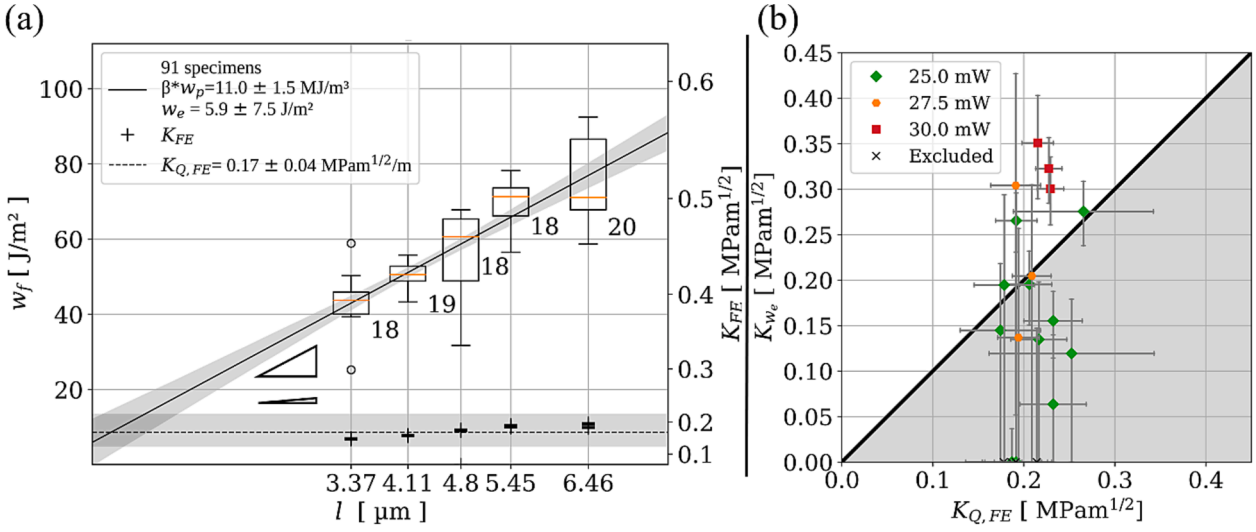

Fig. 9. (a) Results for a PTP grid as shown in Fig. 6, with the specific work of fracture w_f results. On the secondary y-axis the corresponding stress intensity-based values K_{FE} are plotted, obtained using load at fracture and FE simulation obtained geometry factors. The average value is taken as conditional fracture toughness $K_{Q,FE}$ for comparison reasons. (b) Comparison of EWF derived results and $K_{Q,FE}$ for all PTP arrays in terms of stress intensity.

Declaration of Competing Interest

The authors declare that they have no known competing financial interests or personal relationships that could have appeared to influence the work reported in this paper.

Data availability

Data will be made available on request.

Acknowledgements

The infrastructure was funded by the Austrian Research Promotion Agency (FFG) in the framework of the F&E infrastructure program SmartNanoTop (ffg.at) [grant number 870449]. The authors acknowledge funding by the European Research Council [grant number 771146] (DK) and partial funding by the Austrian Science Fund (FWF) [grant number ESP 41-N] (SZ). The authors want to thank Elisabeth Rossegger, from the Polymer Competence Center Leoben GmbH, for her support regarding the preparation of silanized printing substrates.

Appendix A. Supplementary data

Supplementary data to this article can be found online at https://doi.org/10.1016/j.matdes.2023.112329.

References

[1] T. Baghdasaryan, K. Vanmol, H. Thienpont, F. Berghmans, T. Geernaert, J. Van Erps, Design and two-photon direct laser writing of low-loss waveguides, tapers and S-bends, J. Phys. Photonics. 3 (4) (2021), 045001, https://doi.org/10.1088/2515-7647/ac1b7d.

[2] H.H. Duc Nguyen, U. Hollenbach, U. Ostrzinski, K. Pfeiffer, S. Hengsbach, J. Mohr, Freeform three-dimensional embedded polymer waveguides enabled by external-diffusion assisted two-photon lithography, Appl. Opt. 55 (8) (2016) 1906.

[3] A. Bertoncini, C. Liberale, 3D printed waveguides based on photonic crystal fiber designs for complex fiber-end photonic devices, Optica. 7 (2020) 1487, https://doi.org/10.1364/OPTICA.397281.

[4] J. Bürger, J. Kim, B. Jang, J. Gargiulo, M.A. Schmidt, S.A. Maier, Ultrahigh-aspect-ratio light cages: fabrication limits and tolerances of free-standing 3D nanoprinted waveguides, Opt. Mater. Express. 11 (2021) 1046. https://doi.org/10.1364/OME.419398.

[5] P.K. Gill, D.M. Marom, Single Mode, Air-Cladded Optical Waveguides Supported by a Nano-Fin Fabricated with Direct Laser Writing, Appl. Sci. 11 (2021) 6327, https://doi.org/10.3390/app11146327.

[6] H. Gehring, M. Blaicher, W. Hartmann, P. Varytis, K. Busch, M. Wegener, W.H.P. Pernice, Low-loss fiber-to-chip couplers with ultrawide optical bandwidth, APL Photonics. 4 (2019) 010801. https://doi.org/10.1063/1.5064401.

[7] A. Landowski, D. Zepp, S. Wingerter, G. von Freymann, A. Widera, Direct laser written polymer waveguides with out of plane couplers for optical chips, APL Photonics. 2 (2017) 106102. https://doi.org/10.1063/1.4994806.

[8] K. Vanmol, K. Saurav, V. Panapakkam, H. Thienpont, N. Vermeulen, J. Watte, J. Van Erps, Mode-field Matching Down-Tapers on Single-Mode Optical Fibers for Edge Coupling Towards Generic Photonic Integrated Circuit Platforms, J. Lightwave Technol. 38 (2020) 4834–4842, https://doi.org/10.1109/JLT.2020.2997090.

[9] K. Vanmol, T. Baghdasaryan, N. Vermeulen, K. Saurav, J. Watté, H. Thienpont, J. Van Erps, 3D direct laser writing of microstructured optical fiber tapers on single-mode fibers for mode-field conversion, Opt. Express 28 (2020) 36147, https://doi.org/10.1364/OE.409148.

[10] W. Hartmann, P. Varytis, H. Gehring, N. Walter, F. Beutel, K. Busch, W. Pernice, Waveguide-Integrated Broadband Spectrometer Based on Tailored Disorder, Adv. Optical Mater. 8 (2020) 1901602, https://doi.org/10.1002/adom.201901602.

[11] H. Gehring, M. Blaicher, T. Grottke, W.H.P. Pernice, Reconfigurable Nanophotonic Circuitry Enabled by Direct-Laser-Writing, IEEE J. Select. Topics Quantum Electron. 26 (2020) 1–5, https://doi.org/10.1109/JSTQE.2020.3004278.

[12] J. Feldmann, N. Youngblood, M. Karpov, H. Gehring, X. Li, M. Stappers, M. Le Gallo, X. Fu, A. Lukashchuk, A.S. Raja, J. Liu, C.D. Wright, A. Sebastian, T. J. Kippenberg, W.H.P. Pernice, H. Bhaskaran, Parallel convolutional processing using an integrated photonic tensor core, Nature 589 (2021) 52–58, https://doi.org/10.1038/s41586-020-03070-1.

[13] F. Beutel, H. Gehring, M.A. Wolff, C. Schuck, W. Pernice, Detector-integrated on-chip QKD receiver for GHz clock rates, NPJ Quantum Inf. 7 (2021) 40, https://doi.org/10.1038/s41534-021-00373-7.

[14] M. Blaicher, M.R. Billah, J. Kemal, T. Hoose, P. Marin-Palomo, A. Hofmann, Y. Kutuvantavida, C. Kieninger, P.-I. Dietrich, M. Lauermann, S. Wolf, U. Troppenz, M. Moehrle, F. Merget, S. Skacel, J. Witzens, S. Randel, W. Freude, C. Koos, Hybrid multi-chip assembly of optical communication engines by in situ 3D nano-lithography, Light Sci. Appl. 9 (2020) 71, https://doi.org/10.1038/s41377-020-0272-5.

[15] C.R. Ocier, C.A. Richards, D.A. Bacon-Brown, Q. Ding, R. Kumar, T.J. Garcia, J. van de Groep, J.-H. Song, A.J. Cyphersmith, A. Rhode, A.N. Perry, A. J. Littlefield, J. Zhu, D. Xie, H. Gao, J.F. Messinger, M.L. Brongersma, K. C. Toussaint, L.L. Goddard, P.V. Braun, Direct laser writing of volumetric gradient index lenses and waveguides, Light Sci. Appl. 9 (2020) 196, https://doi.org/10.1038/s41377-020-00431-3.

[16] T. Gissibl, S. Thiele, A. Herkommer, H. Giessen, Sub-micrometre accurate free-form optics by three-dimensional printing on single-mode fibres, Nat. Commun. 7 (2016) 11763, https://doi.org/10.1038/ncomms11763.

[17] T. Gissibl, M. Schmid, H. Giessen, Spatial beam intensity shaping using phase masks on single-mode optical fibers fabricated by femtosecond direct laser writing, Optica. 3 (2016) 448, https://doi.org/10.1364/OPTICA.3.000448.

[18] K. Vanmol, S. Tuccio, V. Panapakkam, H. Thienpont, J. Watté, J. Van Erps, Two-photon direct laser writing of beam expansion tapers on single-mode optical fibers, Opt. Laser Technol. 112 (2019) 292–298, https://doi.org/10.1016/j.optlastec.2018.11.028.

[19] W. Hadibrata, H. Wei, S. Krishnaswamy, K. Aydin, Inverse Design and 3D Printing of a Metalens on an Optical Fiber Tip for Direct Laser Lithography, Nano Lett. 21 (2021) 2422–2428, https://doi.org/10.1021/acs.nanolett.0c04463.

[20] J.C. Williams, H. Chandrahalim, J.S. Suelzer, N.G. Usechak, Two-Photon Nanomachining of a Micromechanically Enhanced Optical Cavity Sensor on an Optical Fiber Tip, Advanced Photonics Research. 3 (2022) 2100359, https://doi.org/10.1002/adpr.202100359.

[21] J.A. Kim, D.J. Wales, A.J. Thompson, G. Yang, Fiber-Optic SERS Probes Fabricated Using Two-Photon Polymerization For Rapid Detection of Bacteria, Adv. Optical Mater. 8 (2020) 1901934, https://doi.org/10.1002/adom.201901934.

[22] S. Cao, X. Shang, H. Yu, L. Shi, L. Zhang, N. Wang, M. Qiu, Two-photon direct laser writing of micro Fabry-Perot cavity on single-mode fiber for refractive index sensing, Opt. Express. 30 (2022) 25536. https://doi.org/10.1364/OE.464210.

[23] M. Chen, Y. Zhao, H. Wei, C. Zhu, S. Krishnaswamy, 3D printed castle style Fabry-Perot microcavity on optical fiber tip as a highly sensitive humidity sensor, Sens. Actuators B 328 (2021), 128981, https://doi.org/10.1016/j.snb.2020.128981.

[24] D. Zhang, H. Wei, H. Hu, S. Krishnaswamy, Highly sensitive magnetic field microsensor based on direct laser writing of fiber-tip optofluidic Fabry-Pérot cavity, APL Photonics 5 (7) (2020), 076112, https://doi.org/10.1063/5.0012988.

[25] J. Li, S. Thiele, B.C. Quirk, R.W. Kirk, J.W. Verjans, E. Akers, C.A. Bursill, S. J. Nicholls, A.M. Herkommer, H. Giessen, R.A. McLaughlin, Ultrathin monolithic 3D printed optical coherence tomography endoscopy for preclinical and clinical use, Light Sci. Appl. 9 (2020) 124, https://doi.org/10.1038/s41377-020-00365-w.

[26] K. Moussi, A.A. Haneef, R.A. Alsiary, E.M. Diallo, M.A. Boone, H. Abu-Araki, O. O. Al-Radi, J. Kosel, A Microneedles Balloon Catheter for Endovascular Drug Delivery, Adv. Mater. Technol. 6 (2021) 2100037, https://doi.org/10.1002/admt.202100037.

[27] B. Szeto, A. Aksit, C. Valentini, M. Yu, E.G. Werth, S. Goeta, C. Tang, L.M. Brown, E.S. Olson, J.W. Kysar, A.K. Lalwani, Novel 3D-printed hollow microneedles facilitate safe, reliable, and informative sampling of perilymph from guinea pigs, Hear. Res. 400 (2021), 108141, https://doi.org/10.1016/j.heares.2020.108141.

[28] A. Aksit, D.N. Arteaga, M. Arriaga, X. Wang, H. Watanabe, K.E. Kasza, A. K. Lalwani, J.W. Kysar, In-vitro perforation of the round window membrane via direct 3-D printed microneedles, Biomed. Microdevices 20 (2018) 47, https://doi.org/10.1007/s10544-018-0287-3.

[29] B. Spagnolo, V. Brunetti, G. Leménager, E. De Luca, L. Sileo, T. Pellegrino, P. Paolo Pompa, M. De Vittorio, F. Pisanello, Three-dimensional cage-like microscaffolds for cell invasion studies, Scientific Reports 5 (2015) 10531, https://doi.org/10.1038/srep10531.

[30] A. Erben, M. Hörning, B. Hartmann, T. Becke, S.A. Eisler, A. Southan, S. Cranz, O. Hayden, N. Kneidinger, M. Königshoff, M. Lindner, G.E.M. Tovar, G. Burgstaller, H. Clausen-Schaumann, S. Sudhop, M. Heymann, Precision 3D-Printed Cell Scaffolds Mimicking Native Tissue Composition and Mechanics, Adv. Healthc. Mater. 9 (2020) 2000918, https://doi.org/10.1002/adhm.202000918.

[31] S.H. Yagoub, J.G. Thompson, A. Orth, K. Dholakia, B.C. Gibson, K.R. Dunning, Fabrication on the microscale: a two-photon polymerized device for oocyte microinjection, J. Assist. Reprod. Genet. 39 (2022) 1503–1513, https://doi.org/10.1007/s10815-022-02485-1.

[32] F. Larramendy, S. Yoshida, D. Maier, Z. Fekete, S. Takeuchi, O. Paul, 3D arrays of microcages by two-photon lithography for spatial organization of living cells, Lab Chip 19 (2019) 875–884, https://doi.org/10.1039/C8LC01240G.

[33] J. Kim, B. Jang, T. Wieduwilt, S.C. Warren-Smith, J. Bürger, S.A. Maier, M.A. Schmidt, On-chip fluorescence detection using photonic bandgap guiding optofluidic hollow-core light cage, APL Photonics. 7 (2022) 106103. https://doi.org/10.1063/5.0102071.

[34] J. Lölsberg, J. Linkhorst, A. Cinar, A. Jans, A.J.C. Kuehne, M. Wessling, 3D Nanofabrication inside rapid prototyped microfluidic channels showcased by wet-spinning of single micrometre fibres, Lab Chip 18 (2018) 1341–1348, https://doi.org/10.1039/C7LC01366C.

[35] S. Reede, I. Eichhorn, M. Oellers, A. Schander, M.J. Vellekoop, Two-Photon Polymerized Flow Sensor Integrated in a Microfluidic Channel with

Optoelectronic Readout, in: 2020 IEEE SENSORS, IEEE, Rotterdam, Netherlands, 2020: pp. 1–4. https://doi.org/10.1109/SENSORS47125.2020.9278690.
[36] J.A. Wippold, C. Huang, D. Stratis-Cullum, A. Han, Enhancing droplet transition capabilities using sloped microfluidic channel geometry for stable droplet operation, Biomed. Microdevices 22 (2020) 15, https://doi.org/10.1007/s10544-019-0466-x.
[37] Z. Liu, M. Li, X. Dong, Z. Ren, W. Hu, M. Sitti, Creating three-dimensional magnetic functional microdevices via molding-integrated direct laser writing, Nat. Commun. 13 (2022) 2016, https://doi.org/10.1038/s41467-022-29645-2.
[38] C. Michas, M.Ç. Karakan, P. Nautiyal, J.G. Seidman, C.E. Seidman, A. Agarwal, K. Ekinci, J. Eyckmans, A.E. White, C.S. Chen, Engineering a living cardiac pump on a chip using high-precision fabrication, Sci. Adv. 8 (2022) eabm3791, https://doi.org/10.1126/sciadv.abm3791.
[39] R.K. Jayne, M.Ç. Karakan, K. Zhang, N. Pierce, C. Michas, D.J. Bishop, C.S. Chen, K.L. Ekinci, A.E. White, Direct laser writing for cardiac tissue engineering: a microfluidic heart on a chip with integrated transducers, Lab Chip 21 (2021) 1724–1737, https://doi.org/10.1039/D0LC01078B.
[40] J. Bauer, A. Guell Izard, Y. Zhang, T. Baldacchini, L. Valdevit, Programmable Mechanical Properties of Two-Photon Polymerized Materials: From Nanowires to Bulk, Adv. Mater. Technol. 4 (2019) 1900146, https://doi.org/10.1002/admt.201900146.
[41] J.S. Oakdale, J. Ye, W.L. Smith, J. Biener, Post-print UV curing method for improving the mechanical properties of prototypes derived from two-photon lithography, Opt. Express 24 (2016) 27077, https://doi.org/10.1364/OE.24.027077.
[42] R.K. Jayne, T.J. Stark, J.B. Reeves, D.J. Bishop, A.E. White, Dynamic Actuation of Soft 3D Micromechanical Structures Using Micro-Electromechanical Systems (MEMS), Adv. Mater. Technol. 3 (2018) 1700293, https://doi.org/10.1002/admt.201700293.
[43] N. Rohbeck, R. Ramachandramoorthy, D. Casari, P. Schürch, T.E.J. Edwards, L. Schilinsky, L. Philippe, J. Schwiedrzik, J. Michler, Effect of high strain rates and temperature on the micromechanical properties of 3D-printed polymer structures made by two-photon lithography, Mater. Des. 195 (2020), 108977, https://doi.org/10.1016/j.matdes.2020.108977.
[44] J.R. White, Polymer ageing: physics, chemistry or engineering? Time to reflect, Comptes Rendus Chimie. 9 (2006) 1396–1408, https://doi.org/10.1016/j.crci.2006.07.008.
[45] J. Bauer, A.G. Izard, Y. Zhang, T. Baldacchini, L. Valdevit, Thermal post-curing as an efficient strategy to eliminate process parameter sensitivity in the mechanical properties of two-photon polymerized materials, Opt. Express 28 (2020) 20362, https://doi.org/10.1364/OE.395986.
[46] E.D. Lemma, F. Rizzi, T. Dattoma, B. Spagnolo, L. Sileo, A. Qualtieri, M. De Vittorio, F. Pisanello, Mechanical properties tunability of three-dimensional polymeric structures in two-photon lithography, IEEE Trans. Nanotechnology. (2016) 1–1. https://doi.org/10.1109/TNANO.2016.2625820.
[47] D. Kiener, W. Grosinger, G. Dehm, R. Pippan, A further step towards an understanding of size-dependent crystal plasticity: In situ tension experiments of miniaturized single-crystal copper samples, Acta Mater. 56 (2008) 580–592, https://doi.org/10.1016/j.actamat.2007.10.015.
[48] A. Reichardt, M. Ionescu, J. Davis, L. Edwards, R.P. Harrison, P. Hosemann, D. Bhattacharyya, In situ micro tensile testing of He+2 ion irradiated and implanted single crystal nickel film, Acta Mater. 100 (2015) 147–154, https://doi.org/10.1016/j.actamat.2015.08.028.
[49] R. Kellman, Research Corporation and John Schaefer, Science. 306 (2004) 1133–1133. https://doi.org/10.1126/science.306.5699.1133c.
[50] M.D. Uchic, P.A. Shade, D.M. Dimiduk, Micro-compression testing of fcc metals: A selected overview of experiments and simulations, JOM 61 (2009) 36–41, https://doi.org/10.1007/s11837-009-0038-2.
[51] C. Kirchlechner, F. Toth, F.G. Rammerstorfer, F.D. Fischer, G. Dehm, Pre- and post-buckling behavior of bi-crystalline micropillars: Origin and consequences, Acta Mater. 124 (2017) 195–203, https://doi.org/10.1016/j.actamat.2016.10.075.
[52] G. Dehm, B.N. Jaya, R. Raghavan, C. Kirchlechner, Overview on micro- and nanomechanical testing: New insights in interface plasticity and fracture at small length scales, Acta Mater. 142 (2018) 248–282, https://doi.org/10.1016/j.actamat.2017.06.019.
[53] J.G. Gigax, H. Vo, Q. McCulloch, M. Chancey, Y. Wang, S.A. Maloy, N. Li, P. Hosemann, Micropillar compression response of femtosecond laser-cut single crystal Cu and proton irradiated Cu, Scr. Mater. 170 (2019) 145–149, https://doi.org/10.1016/j.scriptamat.2019.05.004.
[54] R. Pippan, S. Wurster, D. Kiener, Fracture mechanics of micro samples: Fundamental considerations, Mater. Des. 159 (2018) 252–267, https://doi.org/10.1016/j.matdes.2018.09.004.
[55] M. Alfreider, D. Kozic, O. Kolednik, D. Kiener, In-situ elastic-plastic fracture mechanics on the microscale by means of continuous dynamical testing, Mater. Des. 148 (2018) 177–187, https://doi.org/10.1016/j.matdes.2018.03.051.
[56] J. Ast, M. Ghidelli, K. Durst, M. Göken, M. Sebastiani, A.M. Korsunsky, A review of experimental approaches to fracture toughness evaluation at the micro-scale, Mater. Des. 173 (2019), 107762, https://doi.org/10.1016/j.matdes.2019.107762.
[57] M. Alfreider, S. Kolitsch, S. Wurster, D. Kiener, An analytical solution for the correct determination of crack lengths via cantilever stiffness, Mater. Des. 194 (2020), 108914, https://doi.org/10.1016/j.matdes.2020.108914.
[58] A.J. Durelli, S. Morse, V. Parks, The theta specimen for determining tensile strength of brittle materials, Mat. Res. and Stand. 2 (1962) 114–117.
[59] G.D. Quinn, E. Fuller, D. Xiang, A. Jillavenkatesa, L. Ma, D. Smith, J. Beall, A Novel Test Method for Measuring Mechanical Properties at the Small-Scale: The Theta Specimen, in: E. Lara-Curzio (Ed.), Ceramic Engineering and Science Proceedings, John Wiley & Sons Inc, Hoboken, NJ, USA, 2005, pp. 117–126, https://doi.org/10.1002/9780470291221.ch15.
[60] M.S. Gaither, F.W. DelRio, R.S. Gates, E.R. Fuller, R.F. Cook, Strength distribution of single-crystal silicon theta-like specimens, Scr. Mater. 63 (4) (2010) 422–425.
[61] J. Bauer, A. Schroer, R. Schwaiger, I. Tesari, C. Lange, L. Valdevit, O. Kraft, Push-to-pull tensile testing of ultra-strong nanoscale ceramic–polymer composites made by additive manufacturing, Extreme Mech. Lett. 3 (2015) 105–112, https://doi.org/10.1016/j.eml.2015.03.006.
[62] L.R. Meza, A.J. Zelhofer, N. Clarke, A.J. Mateos, D.M. Kochmann, J.R. Greer, Resilient 3D hierarchical architected metamaterials, PNAS 112 (2015) 11502–11507, https://doi.org/10.1073/pnas.1509120112.
[63] A. Schroer, J.M. Wheeler, R. Schwaiger, Deformation behavior and energy absorption capability of polymer and ceramic-polymer composite microlattices under cyclic loading, J. Mater. Res. 33 (2018) 274–289, https://doi.org/10.1557/jmr.2017.485.
[64] T.L. Anderson, Fracture Mechanics: Fundamentals and Applications, Third Edition, CRC Press, USA, Boca Raton, FL, 2005. https://doi.org/10.1201/9781420058215.
[65] A. Jelinek, S. Zak, M. Alfreider, D. Kiener, High-Throughput Micromechanical Testing Enabled by Optimized Direct Laser Writing, Adv. Eng. Mater. (2022) 2200288, https://doi.org/10.1002/adem.202200288.
[66] B. Cotterell, J.K. Reddel, The essential work of plane stress ductile fracture, Int. J. Fract. 13 (1977) 267–277, https://doi.org/10.1007/BF00040143.
[67] K.B. Broberg, Critical review of some theories in fracture mechanics, Int. J. Fract. 4 (1968) 11–19, https://doi.org/10.1007/BF00189139.
[68] B. Cotterell, T. Pardoen, A.G. Atkins, Measuring toughness and the cohesive stress–displacement relationship by the essential work of fracture concept, Eng. Fract. Mech. 72 (2005) 827–848, https://doi.org/10.1016/j.engfracmech.2004.10.002.
[69] S.K. Chandra, R. Sarkar, A.D. Bhowmick, P.S. De, P.C. Chakraborti, S.K. Ray, Fracture toughness evaluation of interstitial free steel sheet using Essential Work of Fracture (EWF) method, Eng. Fract. Mech. 204 (2018) 29–45, https://doi.org/10.1016/j.engfracmech.2018.09.026.
[70] T. Bárány, T. Czigány, J. Karger-Kocsis, Application of the essential work of fracture (EWF) concept for polymers, related blends and composites: A review, Progress in Polymer Science. 35 (2010) 1257–1287, https://doi.org/10.1016/j.progpolymsci.2010.07.001.
[71] J. Karger-Kocsis, Microstructural and molecular dependence of the work of fracture parameters in semicrystalline and amorphous polymer systems, in, European Structural Integrity Society, Elsevier (2000) 213–230, https://doi.org/10.1016/S1566-1369(00)80020-5.
[72] C. Bandl, N. Krempl, G. Berger-Weber, W. Kern, W. Friesenbichler, Application of organosilane coatings for improved anti-adhesive properties enabling facilitated demolding in polymer processing, J. Appl. Polym. Sci. 138 (2021) 50714, https://doi.org/10.1002/app.50714.
[73] M.J. Pfeifenberger, M. Mangang, S. Wurster, J. Reiser, A. Hohenwarter, W. Pfleging, D. Kiener, R. Pippan, The use of femtosecond laser ablation as a novel tool for rapid micro-mechanical sample preparation, Mater. Des. 121 (2017) 109–118, https://doi.org/10.1016/j.matdes.2017.02.012.
[74] A.B. Martinez, J. Gamez-Perez, M. Sanchez-Soto, J.I. Velasco, O.O. Santana, M. Ll Maspoch, The Essential Work of Fracture (EWF) method – Analyzing the Post-Yielding Fracture Mechanics of polymers, Eng. Fail. Anal. 16 (2009) 2604–2617, https://doi.org/10.1016/j.engfailanal.2009.04.027.
[75] A. Milovanović, A. Sedmak, Z. Golubović, K.Z. Mihajlović, A. Žurkić, I. Trajković, M. Milošević, The effect of time on mechanical properties of biocompatible photopolymer resins used for fabrication of clear dental aligners, J. Mech. Behav. Biomed. Mater. 119 (2021), 104494, https://doi.org/10.1016/j.jmbbm.2021.104494.
[76] M. Reymus, B. Stawarczyk, In vitro study on the influence of postpolymerization and aging on the Martens parameters of 3D-printed occlusal devices, J. Prosthet. Dent. 125 (2021) 817–823, https://doi.org/10.1016/j.prosdent.2019.12.026.
[77] Y.-W. Mai, P. Powell, Essential work of fracture and j-integral measurements for ductile polymers, J. Polym. Sci. B Polym. Phys. 29 (1991) 785–793, https://doi.org/10.1002/polb.1991.090290702.
[78] Y.-W. Mai, B. Cotterell, On the essential work of ductile fracture in polymers, Int. J. Fract. 32 (1986) 105–125, https://doi.org/10.1007/BF00019787.
[79] X. Chen, Y.-W. Mai, P. Tong, L. Zhang, Numerical simulation of the essential fracture work method, in, European Structural Integrity Society, Elsevier (2000) 175–186, https://doi.org/10.1016/S1566-1369(00)80017-5.
[80] B. Moser, K. Wasmer, L. Barbieri, J. Michler, Strength and fracture of Si micropillars: A new scanning electron microscopy-based micro-compression test, J. Mater. Res. 22 (2007) 1004–1011, https://doi.org/10.1557/jmr.2007.0140.
[81] J.T. Pürstl, H.O. Jones, T.E.J. Edwards, R.P. Thompson, F. Di Gioacchino, N. G. Jones, W.J. Clegg, On the extraction of yield stresses from micro-compression experiments, Mater. Sci. Eng. A 800 (2021), 140323, https://doi.org/10.1016/j.msea.2020.140323.
[82] M. Alfreider, M. Meindlhumer, V. Maier-Kiener, A. Hohenwarter, D. Kiener, Extracting information from noisy data: strain mapping during dynamic in situ SEM experiments, J. Mater. Res. 36 (2021) 2291–2304, https://doi.org/10.1557/s43578-020-00041-0.
[83] S.S. Mousavi, M.R.M. Aliha, D.M. Imani, On the use of edge cracked short bend beam specimen for PMMA fracture toughness testing under mixed-mode I/II,

Polym. Test. 81 (2020), 106199, https://doi.org/10.1016/j.polymertesting.2019.106199.
[84] A.B. Martínez, A. Segovia, J. Gamez-Perez, M. Ll, Maspoch, Influence of femtolaser notch sharpening technique in the determination of essential work of fracture (EWF) parameters, Eng. Fract. Mech. 76 (2009) 1247–1254, https://doi.org/10.1016/j.engfracmech.2009.01.015.
[85] J.G. Williams, M. Rink, The standardisation of the EWF test, Eng. Fract. Mech. 74 (2007) 1009–1017, https://doi.org/10.1016/j.engfracmech.2006.12.017.
[86] D. Kim, J.-S. Shim, D. Lee, S.-H. Shin, N.-E. Nam, K.-H. Park, J.-S. Shim, J.-E. Kim, Effects of Post-Curing Time on the Mechanical and Color Properties of Three-Dimensional Printed Crown and Bridge Materials, Polymers 12 (2020) 2762, https://doi.org/10.3390/polym12112762.
[87] S. Hashemi, Fracture toughness evaluation of ductile polymeric films, J. Mater. Sci. 32 (1997) 1563–1573, https://doi.org/10.1023/A:1018582707419.
[88] A.S. Saleemi, J.A. Nairn, The plane-strain essential work of fracture as a measure of the fracture toughness of ductile polymers, Polym. Eng. Sci. 30 (1990) 211–218, https://doi.org/10.1002/pen.760300404.
[89] J. Wu, Y.-W. Mai, The essential fracture work concept for toughness measurement of ductile polymers, Polym. Eng. Sci. 36 (1996) 2275–2288, https://doi.org/10.1002/pen.10626.
[90] I. Tarhouni, D. Frómeta, D. Casellas, J. Costa, P. Maimí, Assessing the effect of the experimental parameters in the evaluation of the essential work of fracture in high-strength thin sheets, Eng. Fract. Mech. 270 (2022), 108560, https://doi.org/10.1016/j.engfracmech.2022.108560.
[91] Y. Marchal, J.-F. Walhin, F. Delannay, Statistical procedure for improving the precision of the measurement of the essential work of fracture of thin sheets, Int. J. Fract. 87 (1997) 189–199, https://doi.org/10.1023/A:1007482121146.
[92] K. Duan, X. Hu, G. Stachowiak, Modified essential work of fracture model for polymer fracture, Compos. Sci. Technol. 66 (2006) 3172–3178, https://doi.org/10.1016/j.compscitech.2005.02.020.
[93] R. Hill, On discontinuous plastic states, with special reference to localized necking in thin sheets, J. Mech. Phys. Solids 1 (1952) 19–30, https://doi.org/10.1016/0022-5096(52)90003-3.
[94] E.Q. Clutton, ESIS TC4 experience with the essential work of fracture method, in: European Structural Integrity Society, Elsevier, 2000, pp. 187–199, https://doi.org/10.1016/S1566-1369(00)80018-7.
[95] E. Clutton, Essential work of fracture, in: D.R. Moore, A. Pavan, J.G. Williams (Eds.), European Structural Integrity Society, Elsevier, 2001: pp. 177–195. https://doi.org/10.1016/S1566-1369(01)80033-9.
[96] R. Knockaert, I. Doghri, Y. Marchal, T. Pardoen, F. Delannay, Experimental and numerical investigation of fracture in double-edge notched steel plates, Int. J. Fract. 81 (1996) 383–399, https://doi.org/10.1007/BF00012430.
[97] A. Hilhorst, T. Pardoen, P.J. Jacques, Optimization of the essential work of fracture method for characterization of the fracture resistance of metallic sheets, Eng. Fract. Mech. 268 (2022), 108442, https://doi.org/10.1016/j.engfracmech.2022.108442.
[98] C.F. Shih, M.D. German, V. Kumar, An engineering approach for examining crack growth and stability in flawed structures, Int. J. Press. Vessel. Pip. 9 (1981) 159–196, https://doi.org/10.1016/0308-0161(81)90001-6.
[99] A.M.D.S. Melo, A.T.L.D. Caldas, J.D.N. Dias, B.C.D. Borges, I.V.D. Assunção, Mechanical properties and dentin bonding of semi-direct restorations produced with a diatomite-based resin composite, Int. J. Adhes. Adhes. 123 (2023), 103357, https://doi.org/10.1016/j.ijadhadh.2023.103357.
[100] N. Ilie, K. Kunzelmann, R. Hickel, Evaluation of micro-tensile bond strengths of composite materials in comparison to their polymerization shrinkage, Dent. Mater. 22 (2006) 593–601, https://doi.org/10.1016/j.dental.2005.05.014.
[101] H. Watanabe, S. Khera, M. Vargas, F. Qian, Fracture toughness comparison of six resin composites, Dent. Mater. 24 (2008) 418–425, https://doi.org/10.1016/j.dental.2007.06.018.
[102] M.R.M. Aliha, S.S. Samareh-Mousavi, M.M. Mirsayar, Loading rate effect on mixed mode I/II brittle fracture behavior of PMMA using inclined cracked SBB specimen, Int. J. Solids Struct. 232 (2021), 111177, https://doi.org/10.1016/j.ijsolstr.2021.111177.
[103] K. Mishra, L. Brassart, A. Singh, Rate dependent fracture behavior of highly cross-linked epoxy resin, Eng. Fail. Anal. 140 (2022), 106558, https://doi.org/10.1016/j.engfailanal.2022.106558.
[104] M.Y. Abdellah, A.-R. Zuwawi, S.A. Azam, M.K. Hassan, A Comparative Study to Evaluate the Essential Work of Fracture to Measure the Fracture Toughness of Quasi-Brittle Material, Materials. 15 (2022) 4514, https://doi.org/10.3390/ma15134514.
[105] M. Rink, L. Andena, C. Marano, The essential work of fracture in relation to J-integral, Eng. Fract. Mech. 127 (2014) 46–55, https://doi.org/10.1016/j.engfracmech.2014.05.006.